NAVAL POSTGRADUATE SCHOOL

MONTEREY, CALIFORNIA

THESIS

OBSERVED AND SIMULATED TEMPORAL AND SPATIAL VARIATIONS OF GAP OUTFLOW REGION

by

Robin Corey Cherrett

September 2006

Thesis Advisor:	Qing Wang
Second Reader:	Wendell A. Nuss

Approved for public release; distribution is unlimited

THIS PAGE INTENTIONALLY LEFT BLANK

REPORT DOCUMENTATION PAGE		*Form Approved OMB No. 0704-0188*
Public reporting burden for this collection of information is estimated to average 1 hour per response, including the time for reviewing instruction, searching existing data sources, gathering and maintaining the data needed, and completing and reviewing the collection of information. Send comments regarding this burden estimate or any other aspect of this collection of information, including suggestions for reducing this burden, to Washington headquarters Services, Directorate for Information Operations and Reports, 1215 Jefferson Davis Highway, Suite 1204, Arlington, VA 22202-4302, and to the Office of Management and Budget, Paperwork Reduction Project (0704-0188) Washington DC 20503.		
1. AGENCY USE ONLY *(Leave blank)*	**2. REPORT DATE** September 2006	**3. REPORT TYPE AND DATES COVERED** Master's Thesis
4. TITLE AND SUBTITLE Observed and Simulated Temporal and Spatial Variations of Gap Outflow Region		**5. FUNDING NUMBERS**
6. AUTHOR Robin Corey Cherrett		
7. PERFORMING ORGANIZATION NAME(S) AND ADDRESS(ES) Naval Postgraduate School Monterey, CA 93943-5000		**8. PERFORMING ORGANIZATION REPORT NUMBER**
9. SPONSORING /MONITORING AGENCY NAME(S) AND ADDRESS(ES) N/A		**10. SPONSORING/MONITORING AGENCY REPORT NUMBER**
11. SUPPLEMENTARY NOTES The views expressed in this thesis are those of the author and do not reflect the official policy or position of the Department of Defense or the U.S. Government.		
12a. DISTRIBUTION / AVAILABILITY STATEMENT Approved for public release; distribution is unlimited.		**12b. DISTRIBUTION CODE** A

13. ABSTRACT

This study focuses on understanding the development of gap outflow and the air-sea interaction processes during the 26 February 2004 Tehuano event over the Gulf of Tehuantepec, Mexico. The Navy's Coupled Ocean Atmospheric Mesoscale Prediction System (COAMPS^{TM}) was used to simulate the gap wind event and was compared to satellite, scatterometer, and coincident in situ aircraft and dropsondes measurements collected during the Gulf of Tehuantepec Experiment (GOTEX).

Comparisons between model results and the observations suggest that COAMPS^{TM} performed the best in simulating the outflow jet within 200 km offshore, although the simulated surface fluxes deviated significantly from the observations. This is the region where the dominant dynamical forcing arises from the coastal topography. Larger discrepancies were found in model result further away from the coast, especially to the south and southeast of the gulf where the air-sea exchange became increasingly important. Detailed inter-comparison between COAMPS^{TM} and the aircraft measurements at 40 m also shows the strong spatial and temporal variations of boundary layer thermodynamics and turbulence, which require improved characterization of the sea surface temperature, upper air conditions, and initial conditions for COAMPS^{TM}. The results also point to the needs for improved surface flux parameterization, particularly in high wind conditions.

14. SUBJECT TERMS : gap wind, gap outflow, high wind environment, boundary layer evolution, Gulf of Tehuantepec, GOTEX, ocean response, COAMPS, mesoscale, air-sea interaction, surface flux	**15. NUMBER OF PAGES** 79
	16. PRICE CODE

17. SECURITY CLASSIFICATION OF REPORT Unclassified	**18. SECURITY CLASSIFICATION OF THIS PAGE** Unclassified	**19. SECURITY CLASSIFICATION OF ABSTRACT** Unclassified	**20. LIMITATION OF ABSTRACT** UL

NSN 7540-01-280-5500

Standard Form 298 (Rev. 2-89)
Prescribed by ANSI Std. 239-18

i

THIS PAGE INTENTIONALLY LEFT BLANK

**OBSERVED AND SIMULATED
TEMPORAL AND SPATIAL VARIATIONS OF
GAP OUTFLOW REGION**

Robin C. Cherrett
Lieutenant, United States Navy
B.S., University of Washington, 1999

Submitted in partial fulfillment of the
requirements for the degree of

**MASTER OF SCIENCE IN METEOROLOGY AND PHYSICAL
OCEANOGRAPHY**

from the

**NAVAL POSTGRADUATE SCHOOL
September 2006**

Author: Robin Corey Cherrett

Approved by: Qing Wang
                Thesis Advisor

                Wendell A. Nuss
                Second Reader/Co-Advisor

                Philip A. Durkee
                Chairman, Department of Meteorology

iii

THIS PAGE INTENTIONALLY LEFT BLANK

ABSTRACT

This study focuses on understanding the development of gap outflow and the air-sea interaction processes during the 26 February 2004 Tehuano event over the Gulf of Tehuantepec, Mexico. The Navy's Coupled Ocean Atmospheric Mesoscale Prediction System (COAMPS^{TM}) was used to simulate the gap wind event and was compared to satellite, scatterometer, and coincident in situ aircraft and dropsondes measurements collected during the Gulf of Tehuantepec Experiment (GOTEX).

Comparisons between model results and the observations suggest that COAMPS^{TM} performed the best in simulating the outflow jet within 200 km offshore, although the simulated surface fluxes deviated significantly from the observations. This is the region with dominant dynamical forcing arises from the coastal topography. Larger discrepancies were found in model result further away from the coast, especially to the south and southeast of the gulf where the air-sea exchange became increasingly important. Detailed inter-comparison between COAMPS^{TM} and the aircraft measurements at 40 m also shows the strong spatial and temporal variations of boundary layer thermodynamics and turbulence, which require improved characterization of the sea surface temperature, upper air conditions, and initial conditions for COAMPS^{TM}. The results also point to the needs for improved surface flux parameterization, particularly in high wind conditions.

THIS PAGE INTENTIONALLY LEFT BLANK

TABLE OF CONTENTS

THIS PAGE INTENTIONALLY LEFT BLANK

LIST OF FIGURES

x

THIS PAGE INTENTIONALLY LEFT BLANK

ACKNOWLEDGMENTS

THIS PAGE INTENTIONALLY LEFT BLANK

I. INTRODUCTION

A. OVERVIEW

The Sierra Madre mountain range that extends the full length of Mexico and Central America provides a barrier for low level air masses between the Gulf of Mexico and the Pacific Ocean. There are several low level mountain passes that offer a break in the barrier, one of which is the Chivela Pass located in southern Mexico. During the boreal winter season (November to February), frequent and predictable cold surges penetrate southward into Mexico, the Gulf of Mexico, and on into Central America behind vacating low pressure systems that develop on the lee side of the Rocky and Sierra Madre mountain ranges. These cold surges set up a significant cross barrier pressure gradient in southern Mexico. When this occurs, the 40 km narrow channel of Chivela Pass allows flow to cross the barrier and a strong wind event is produced that extends hundreds of kilometers over the Gulf of Tehuantepec and the Eastern Pacific. These gap wind outflow events, known as a 'Tehuano', typically persist for 2 to 6 days with wind speeds of 10 to 20 m s^{-1} (Schultz et al., 1998) and in extreme events, the gusts can exceed 60 m s^{-1} (Stumpf, 1975). The high wind of the Tehuano creates regions of strong mixing and cooling of ocean waters which can lower the sea surface temperature (SST) by as much as 8 ^{o}C in a few hours (Stumpf 1975b; Shultz et al., 1998). As a result, the feedback processes between the lower atmosphere and the upper ocean are significant and strongly time evolving.

Gap wind events, such as the Tehuano, are common in many locations around the world and their effects can have large impacts on military operations of every branch, especially for the Navy. The winds and seas that are produced during these events obviously and immediately impact aviation and surface operations and transit routing. However, the changes in the water mass due to mixing, sea currents due to impulse forcing, and the modification of the boundary layer moisture and temperature profile which change its electro-magnetic and electro-optical propagation characteristics may not be as immediately apparent, but are just the beginning of a list of environmental impacts that affect all areas of naval warfare.

B.   GAP WINDS AND OUTFLOW

Gap winds are low-elevation winds that occur in the channels of the low elevation gaps in a barrier. The cross gap scales can range from hundreds of meters to hundreds of kilometers. As a pressure gradient develops across the region of a gap, low level flow is forced through the limited width of the channel. The restricted flow produces a local increase in wind speeds as well as large changes in the wind direction so that it flows nearly parallel to the channel axis (Figure 1). Larger pressure gradients existing across a gap produce stronger winds through the gap.

Gap wind phenomena are extremely common and many examples exist. A few examples from around the world include Strait of Juan de Fuca between Washington State and Vancouver Island, the Columbia River Gorge through the Cascade Mountains of Oregon and Washington State, the Strait of Gibraltar between Spain and Morocco, and the Luzon Strait between Taiwan and the Philippines among many more.

A thorough discussion of the gap wind formation can be found in http://meted.ucar.edu/mesoprim/gapwinds/ (last visited 15 September 2006). There are three mechanisms that contribute to wind speed acceleration through the gap: the venturi or the funnel effect, synoptic pressure gradient, and the hydraulic effects. The venturi effect describes the flow acceleration through a restriction based on Bernoulli's principle, which results in the strongest flow at the narrowest point of the restriction. Although applicable to small gaps in the range of kilometers or less, the venturi effect is often not the dominant mechanism for most of the gap wind regions in the world. The strongest winds are generally found near the exit region rather than in the narrowest portion of the constriction as would be suggested by the venturi effect. A synoptic scale pressure gradient across the gap and the hydraulic effects, on the other hand, are major mechanisms for gap wind acceleration, particularly at the exit region of the gap.

A typical condition favorable for a gap wind event is when a cool and shallow boundary layer capped by an inversion approaches the gap. As the air mass approaches the barrier, blocking increases the depth of the dense boundary layer which leads to increases in surface pressure. This also tends to slow the flow that is approaching the barrier and gap entrance. The flow is then channeled through the gap. Upon exiting the

gap, the terrain opens and allows the low level air to spread due to pressure acting equally in all directions. As the flow spreads, the boundary layer height decreases which lowers pressure over the exit region. Therefore, accelerations continue to occur where there exists a pressure gradient upon exiting the gap. This effect is referred to as the hydraulic effect.
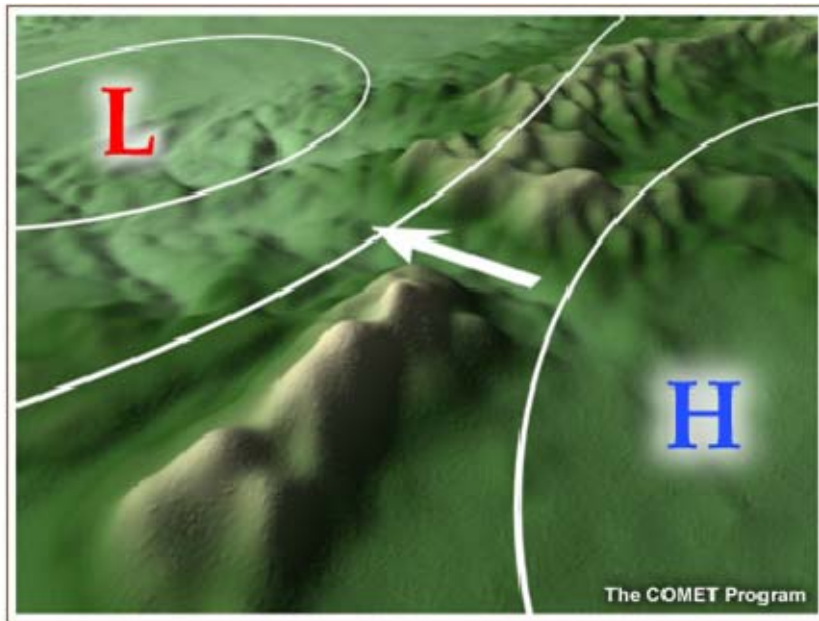
Figure 1.   Schematic shows an anticyclone on one side of a barrier and a low pressure system on the other side of the barrier. The cross barrier flow is forced through the gap and down the pressure gradient which accelerates the winds through the gap (from http://meted.ucar.edu/mesoprim/gapwinds/ last visited September 2006).

Synoptic scale forcing can be a dominant mechanism for the strongest gap wind events. A favorable synoptic condition is when there is an anticyclone on one side of the gap and a low pressure region or cyclone approaches or develops on the other side, resulting in a large pressure gradient across the gap. Generally lesser but still significant pressure gradients along gaps can be associated with a low or high pressure region approaching or developing on one side of the gap.

It is noted that the gap width is normally smaller than the Rossby radius of deformation. Consequently, gap wind is generally ageostrophic and flow is down the pressure gradient.

Gap outflow is then what describes the air after it has exited the gap and is the focus of this study. After the flow has been funneled through the gap, changing direction and speed, a high wind jet is observed to extend from the gap exit for 10s to 100s of km downstream. Some limiting factors to the extent of the outflow jet from the gap exit are synoptic forcing, surface friction, and latitude. Stronger synoptic scale forcing will act upon the outflow quicker than weak or no synoptic forcing through the influence of the pressure gradient (Bourassa et al., 1999). Higher surface friction tends to reduce the momentum of the gap outflow faster than low surface friction (Mass et al., 1995). Higher latitudes will cause the outflow to attain geostrophic balance faster.

Since many gap outflows emerge over water, often the maximum winds will be observed to occur over water downstream from the gap exit. This is due to the reduction of surface friction, instability introduced by cool air over relatively warmer water that promotes mixing of momentum to the surface from the higher winds aloft, and the existence of a pressure gradient near the exit of the gap such as discussed above (Mass et al., 1995).

The outflow then undergoes adjustment until it comes into geostrophic balance with the larger scale pressure field. The trajectory of the jet, in addition to the trajectories of the outflow air parcels, is determined by a balance of the forces enacted on it. Steenburgh et al. (1998) found that the jet will follow an inertial path set by the balance between Coriolis and centrifugal forces. Their study also found that a pressure ridge that exists along the jet core adds another force to the balance of air parcels on either side of the jet. The pressure gradient normal to the jet axis would therefore turn air parcels to the right of the jet more anti-cyclonic than an inertial path would indicate, and would turn air parcels to the left of the jet at a less than inertial path, straight, or even cyclonically. Figure 2 shows the results of their trajectory study, using the MM5 model to simulate the outflow, indicating how the jet spreads and the outflow fans out due to the jet axis pressure ridge and the balance of Coriolis, pressure gradient, and residual forces.
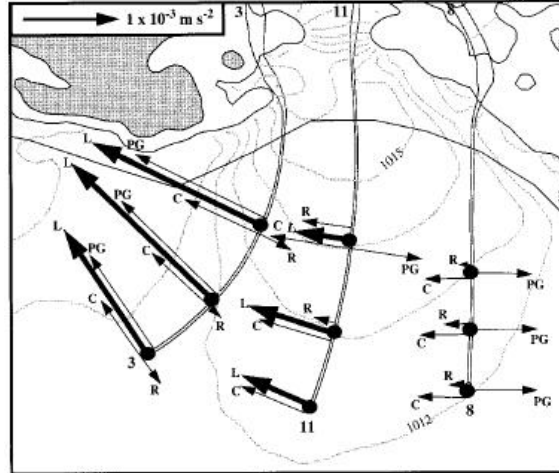
Figure 2.   Cross-flow momentum balance at three sequential hours along three different trajectories. Cross-flow Lagrangian parcel (bold), pressure gradient, Coriolis, and residual acceleration vectors labeled as L, PG, C, and R, respectively. Sea level pressure contours every 1 hPa are drawn for the same time as the calculated momentum balance at the end of the show trajectory (from Steenburgh et al., 1998).

Many gap wind scenarios transpire over a pass through a mountain barrier. Therefore, flow over a sill must also be considered. Over and immediately downwind of Chivela Pass, a wavelike undulation in the isentropes and a region of leeside subsidence were evident in the study by Steenburgh (1998) shown in Figure 3, suggesting a mountain wave had been excited. They also found that a well mixed layer from the surface to about 925 hPa was indicated to be capped by a near isothermal layer that reached to about 875 hPa. The maximum winds were located in these layers. Above the lowest stable layer was a layer of weaker static stability that was also capped by a stable layer at about 725 hPa.

5
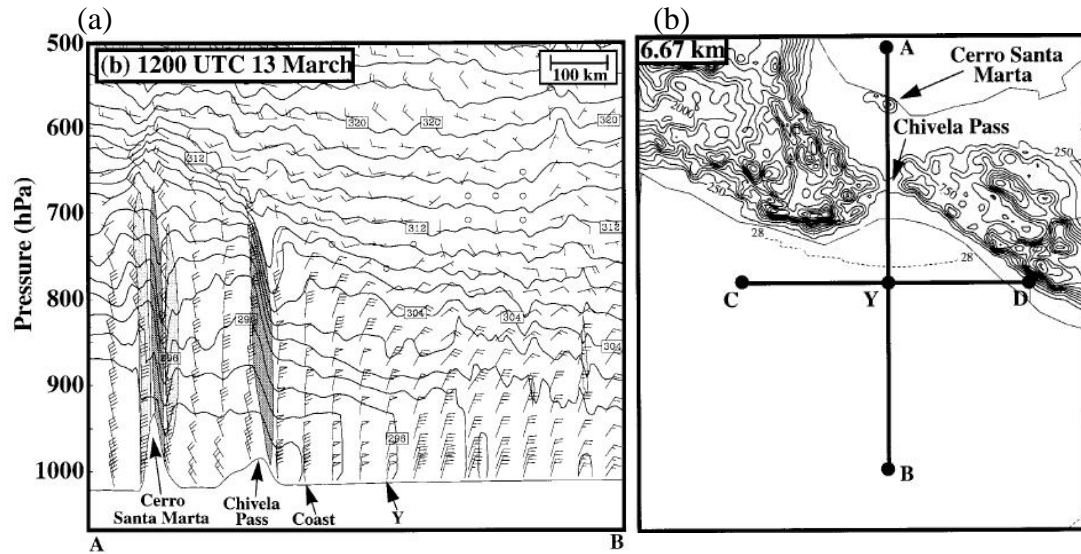
Figure 3.   (a) Cross section plot of potential temperature (every 2^oK) and horizontal wind along line AB. The orientation of cross section AB is shown in (b). The gap flow went from north to south through Chivela Pass. In (a), one pennant, full barb, half barb, and circle denote 25, 5, 2.5, and less than 1.25 m s^{-1}, respectively. Wind barbs oriented so north is toward the top of the page. Light (dark) shading identifies regions of rising (sinking) motion exceeding 0.3 m s^{-1}.(from Steenburgh et al., 1998).

C.   OBJECTIVES

Although the general dynamics of the gap wind field and their interaction with the strong cross-mountain pressure gradients and the local topography have been studied in the past, no research has been done in this region from a perspective of a strongly air-sea coupled system. This is in part due to the lack of in situ observations in this area that makes model validation and evaluation difficult. Yet, the boundary layer processes and air-sea interaction in the area have been recognized as most important factors in determining the evolution of the wind field and the oceanic response, which will be the foci of this thesis study.

This study involves two major components: numerical modeling using the Navy's Coupled Oceanographic Atmospheric Mesoscale Prediction System (COAMPS^{TM}) and observational analysis using data obtained during the Gulf of Tehuantepec Experiment (GOTEX) in 2004. While the aircraft and dropsonde observations allow us to study the fine turbulence structure in a somewhat limited time window and locations, COAMPS^{TM} simulations present the temporal evolution of the development of the gap outflow in three dimensions. In particular, we will focus on one gap wind event on 26–27 February 2004

6

and analyze the spatial variation of the atmospheric boundary and the variations of surface fluxes and turbulent mixing in the boundary layer from both the COAMPS^{TM} simulation and the GOTEX observations.

Chapter II will discuss the geographical region of interest, the operational model set up, and the GOTEX research. The synoptic pattern that produced the gap wind event will be described using a global model analysis and observations from other sources in Chapter III. In Chapter IV, the COAMPS model will be used to describe the mesoscale structure of the Tehuano. Chapter V will analyze the GOTEX data and compare it to the simulated results. Finally, the conclusions and recommendations from this study will be presented in Chapter VI.

THIS PAGE INTENTIONALLY LEFT BLANK

II. BACKGROUND

A. CHIVELA PASS AND THE GULF OF TEHUANTEPEC

The Gulf of Tehuantepec is located on the Pacific side of the Isthmus of Tehuantepec, which is the narrowest part of Mexico between the Gulf of Mexico and the Pacific Ocean. Figure 4 is a topographical representation of the region of interest for this study. The isthmus is about 200 km across at its narrowest point. The Sierra Madre Mountain system of Mexico, with elevations from 1800 m to 3700 m, provides an effective barrier that separates the lower atmosphere between the Gulf of Mexico and the Pacific Ocean. In eastern Mexico, the Sierra Madre Oriental is the mountain range that is an extension of the Rocky Mountains of western Texas and New Mexico and has a median elevation of 2200 m. To the south, the range connects to the Sierra Madre of Oaxaca and the Sierra Madre Del Sur so that the barrier is continuous. In southern Mexico at the location of the Isthmus of Tehuantepec, however, there exists a gap in the mountain range. This gap is called Chivela Pass and has a minimum altitude of only 224 m. To the west of Chivela Pass, the terrain rises gradually to the Sierra Madre of Oaxaca where peaks average 2500 m. To the east, the change in elevation is more abrupt to the average of 1500 m in the Sierra Madre of Chiapas which extends to Guatemala. Therefore, Chivela Pass is the lowest point along this barrier from as far north as Alaska to as far south as Guatemala and provides the low level gap for channeling flow when a pressure gradient exists across Mexico.
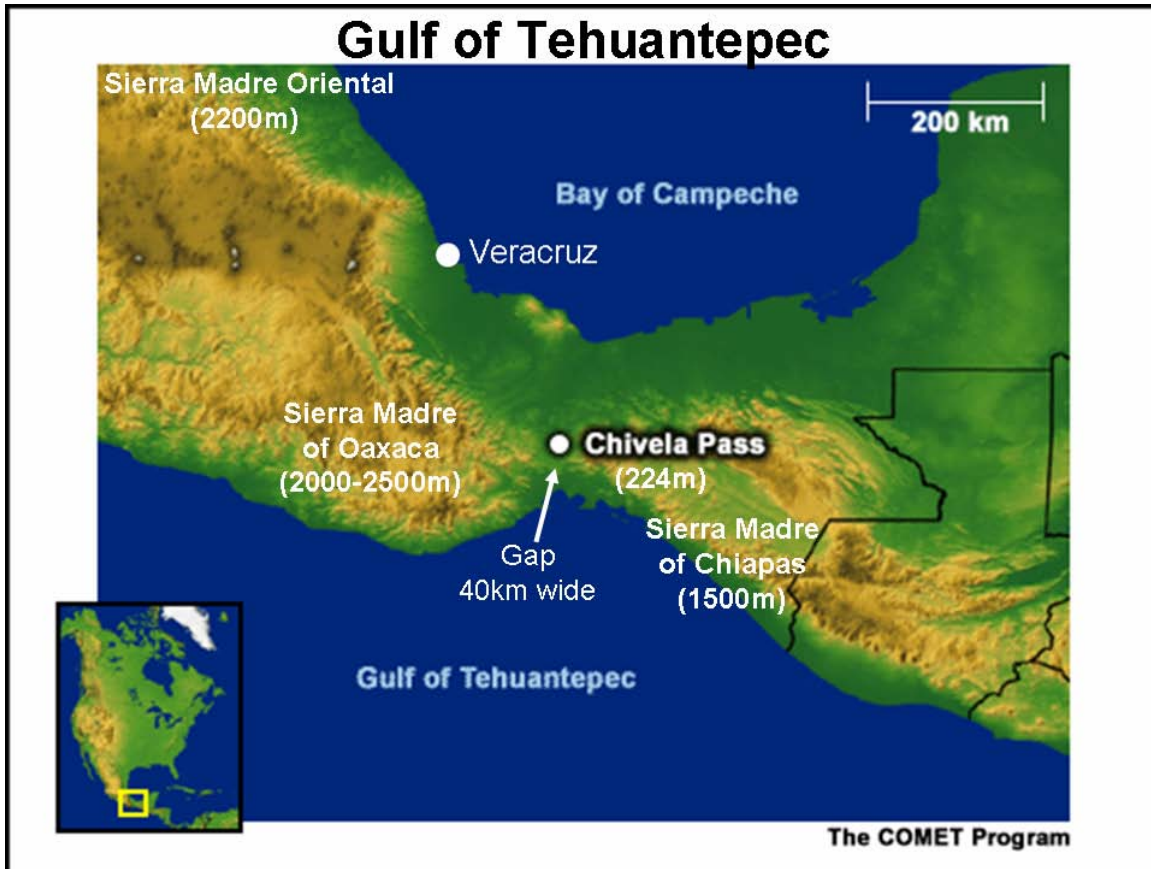
Figure 4.   Terrain map of the Chivela pass, Gulf of Tehuantepec, and surrounding area. Veracruz, located approximately 230 km upwind from the pass, is the location of the sounding in Figures 7 and 9 (From www.comet.ucar.edu Sept 2006).

B.   GULF OF TEHUANTEPEC EXPERIMENT (GOTEX)

GOTEX took place from 1 February to 1 March of 2004 with 11 research flights made by the C130 operated by the National Center for Atmospheric Research (NCAR). Measurements of the GOTEX were designed to study the strong coupling between the atmosphere and ocean in moderate to high wind conditions. In addition to instruments on the aircraft, dropsondes and AXBTs were deployed from 1200 m to profile the marine atmospheric boundary layer (MABL) and the ocean surface mixed layer.   Hence, GOTEX made comprehensive measurements of the lower atmosphere and the surface wave field as well as the ocean mixed layer temperature profiles. This combination of measurements of the development of both the MABL and the wave field, and especially wave breaking, provide considerable further insight into the source functions for the wave field and the air-sea fluxes affecting the developing atmospheric boundary layer.

10

The measurements of the NCAR C130 on 26 February 2004 are used in this study to reveal the near surface thermodynamic and turbulence characteristics in comparison with the COAMPS simulations. In particular, we used the dropsonde measurements of the vertical profiles of the lower atmosphere and the turbulent fluxes of momentum, sensible heat, and latent heat calculated from the high-rate sampled data from the 40 m level legs. The sea surface temperature (SST) from the 40 m leg is also used to identify uncertainties of the COAMPS SST field. All standard instrumentation and data variables on the C130 can be found on http://www.eol.ucar.edu/raf/instruments.html .

C.   COAMPS MODEL DESCRIPTION

The Navy's COAMPS model was used to simulate the gap wind event studied in this thesis. COAMPS is a nonhydrostatic mesoscale model that was designed to be relocatable anywhere in the world. It uses 1 km resolution topography bilinearly interpolated into its mesh grid. SSTs were provided by bilinearly interpolating the Fleet Numerical Meteorology and Oceanography Center (FNMOC) global SST analysis into the COAMPS grids. The boundary conditions were provided by the Navy Operation Global Atmospheric Prediction System (NOGAPS). A detailed description of COAMPS numerical schemes and physical parameterizations can be found in Hodur (1997). As the coupled capability is currently under development, the COAMPS atmospheric model is used.

For this study, three COAMPS nested domains were used at 27 km, 9 km, and 3 km resolution. The results of the finest resolution (3 km) nest are analyzed in this study. In the vertical dimension, 38 z-sigma levels were used with 21 levels below 700 hPa. COAMPS simulations were made by Dr. S. Wang at the Naval Research Laboratory, Monterey, CA. The simulation started on 00Z 25 February 2004 and ends on 12Z 27 February 2004. Each run performed 24 hours of simulation and a new run started every 12 hours with data assimilation turned on. The COAMPS results were saved in "flat files". MATLAB was used to plot the model flat files into horizontal plots, cross sections, and single point model soundings throughout the nest 3 domain to analyze its simulated structure.

11

D. OTHER DATA SOURCES

Data analyses in this study were also augmented by other data sources. These sources included soundings archived by the University of Wyoming, surface weather observations archived by the Plymouth State Weather Center, and upper air conditions from NOGAPS archived at the Fleet Numerical Detachment in Asheville, NC. In addition, satellite visible imagery from GOES East archived by the National Oceanographic and Atmospheric Association (NOAA) and QuickSCAT scatterometry observations of the wind fields archived by the NASA's Jet Propulsion Laboratory were used. Information about QuickSCAT can be found online at http://podaac.jpl.nasa.gov/.

These observations and model results provide the general synoptic conditions and upper air forcing over the gap region and the spatial and temporal evolution of the gap outflow and the upper ocean during the Tehuano event of 26 to 27 February 2004.

III. SYNOPTIC FORCING AND OBSERVED GAP OUTFLOW DEVELOPMENT

A. SYNOPTIC FORCING OF THE GAP FLOW EVENT

Between 25 and 26 February 2004, a strong surge of cold air along the eastern slopes of the Sierra Madre resulted in a strong gap outflow that emerged from Chivela Pass. The lower atmosphere was probed extensively by a research aircraft, the C130, operated by NCAR between approximately 14Z and 22Z. This event will be referred to as GAP022504 and will be the focus of this thesis study. In this chapter, we will first introduce the synoptic conditions that generated this event using results from the NOGAPS, routine meteorological observations, and rawinsonde measurements from nearby weather stations. The development of the gap wind will be shown using Quickscat measured wind fields.

The upper-level conditions preceding GAP022504 can be seen from the 300 hPa geo-height analyses. At 00Z 24 February, the 300 hPa height pattern showed strong high zonal flow over the eastern Pacific leading into split flow just off the California coast to the north and south of a slowly weakening quasi-stationary omega block positioned over the mountain states (Figure 5). The stronger southern branch of that split flow contained a jet streak oriented along the Baja Peninsula of Mexico with winds of 130 kts. The jet streak was approaching a shortwave trough axis located at 110W from New Mexico to Manzanillo, Mexico. This strong jet streak entering the trough was the trigger for the extra-tropical cyclone development that released the cold surge over the Gulf of Mexico and produced this Tehuano event. A subtropical jet also existed from the near equatorial region at 110W over the Gulf of Tehuantepec and combined with the southern branch just east of the trough axis. Some high level cirrus was evident of this subtropical flow in satellite imagery (not shown) along with a weak line of convergence at the surface. At 850 hPa, a temperature gradient of 20 degrees Celsius from the central plains to the Gulf of Mexico provided the baroclinicity for extra-tropical development. At the surface, a high center of 1026 hPa was located over Minnesota. The western Gulf of Mexico was already exhibiting a broad low center of about 1006 hPa located along the Texas and Mexico coastlines. In the Pacific, the subtropical ridge was located at 25N and extended

from the dateline to the Mexican coast with a high center of 1022 hPa located at 140W. This provided synoptic scale flow across most of the eastern Pacific, however, a weak gradient over the area of interest south of Mexico provided relatively little synoptic forcing.
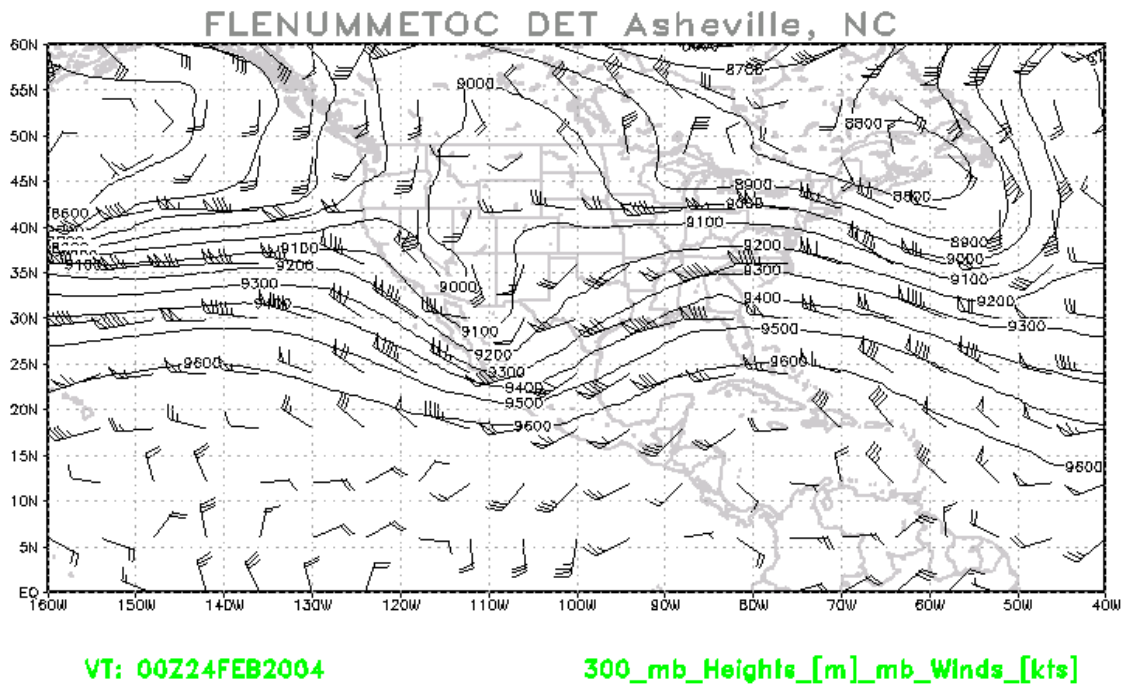
Figure 5.   300 hPa heights and winds for 00Z 24 February 2004.

By 00Z 25 February, the 300 hPa trough had moved east and was located over central Mexico (Figure 6). The broad low center had moved off the coast into the Gulf of Mexico and had deepened slightly to about 1002 hPa. The high center over Minnesota had increased to 1030 hPa and was ridging southwest to the Texas panhandle, building in southward along the mountains filling in behind the cold front that had reached the southern tip of Texas. By 12Z 25 February, northerly winds of 25 kts at 850 hPa were found in the NOGAPS model analysis and verified by soundings at both Brownsville and Corpus Christi, Texas (not shown).
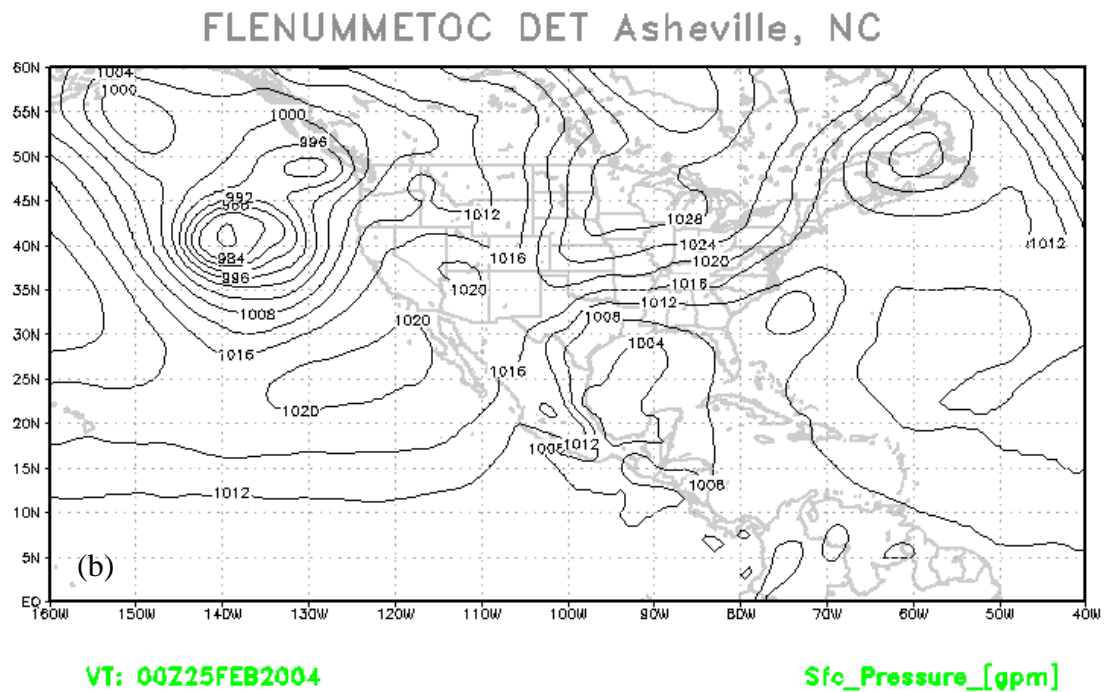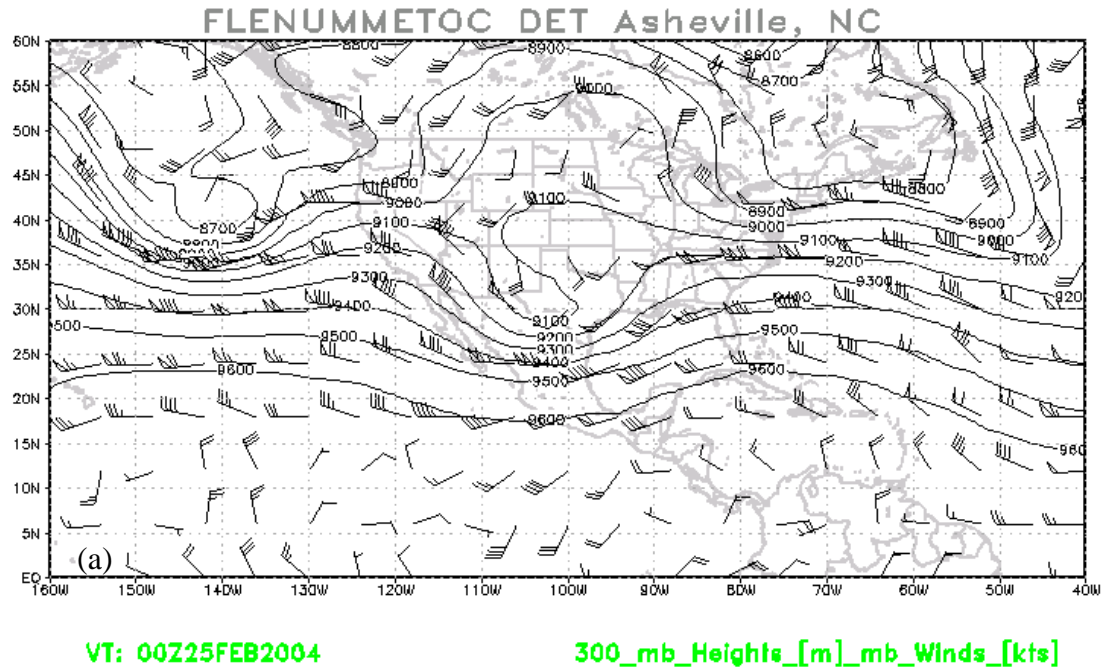
Figure 6. 00Z 25 February NOGAPS analysis for (a)300 hPa heights and winds and (b)surface pressure.

The sounding at Hacienda Ylang Ylang (near Veracruz, Mexico) showed frontal passage already at 12Z 25 February (Figure 7). Frontal passage at Phillip Goldston Intl Airport, Belize (17.53N, 88.3W), indicated by soundings (not shown), occurred between 12Z 25 February and 00Z 26 February.
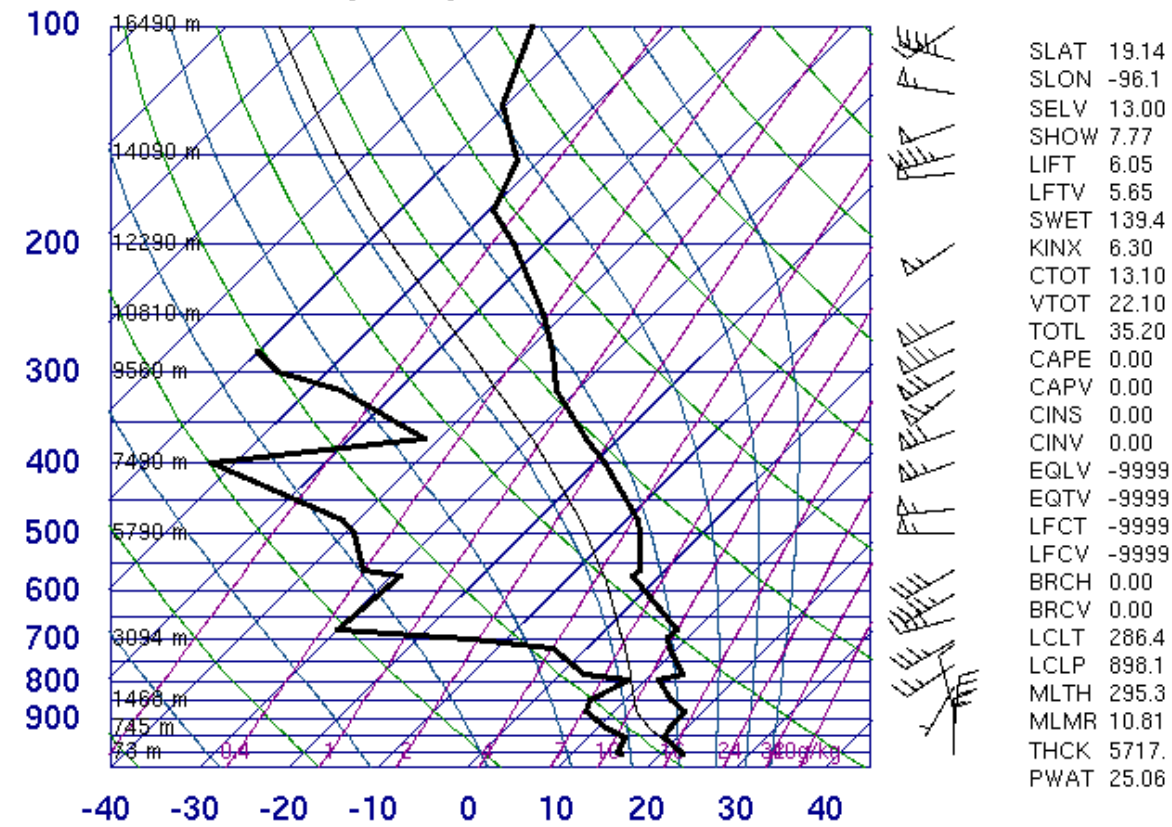
Figure 7.   Sounding near Veracruz, Mexico at 12Z 25 February indicating post frontal passage with northerly winds in the surface layer.

At 12Z 26 February, the Tehuano event was well underway with the cold front having already progressed south to Honduras indicated by the 925 hPa 20 degree isotherm in Figure 8a. The high pressure over the central U.S. extended down the eastern Mexican coast and provided about a six hPa pressure gradient across Chivela pass (Figure 8b). Surface observations along the east coast of Mexico also verified a pressure

16
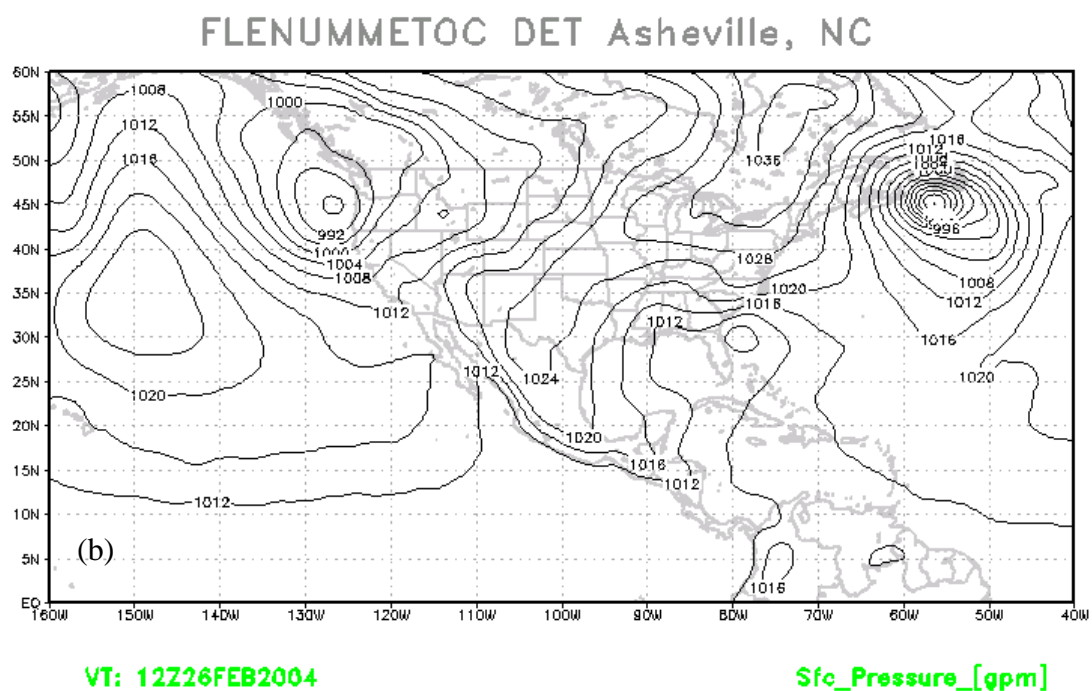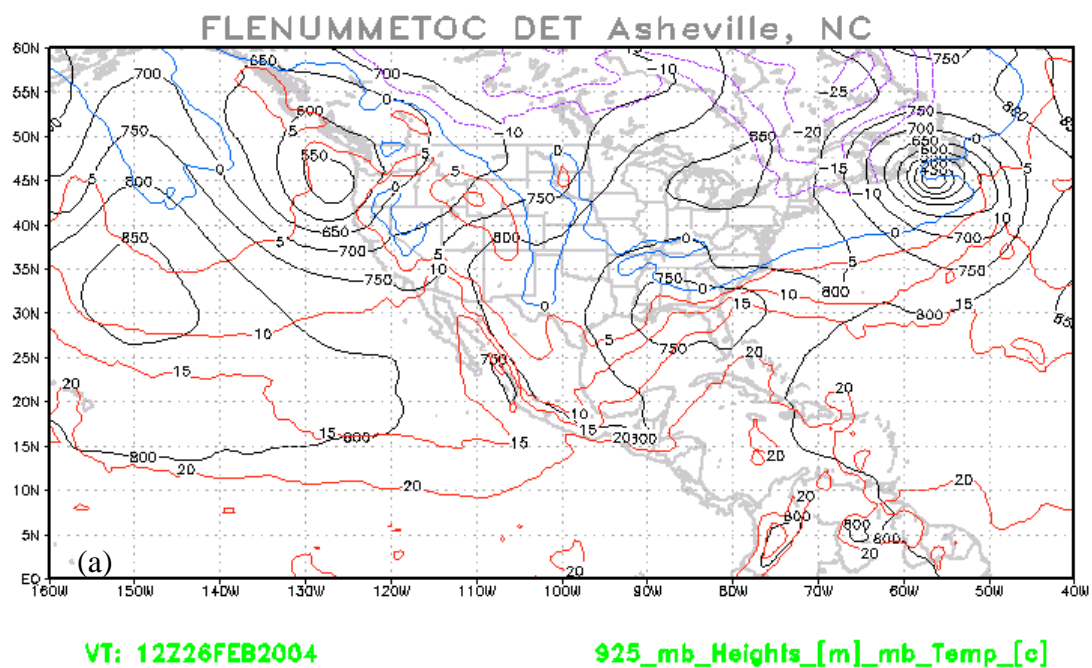
Figure 8.   12Z 26 February (a)925 hPa heights and temperatures and (b)surface
pressure.

rise of about 4 hPa from 18Z 25 February to 12Z 26 February (not shown) Northerly winds and a temperature gradient of about 20 degrees Celsius from central Texas to the south side of Chivela pass continued the advection of cool air behind the front.

The development of the large scale forcing producing the Tehuano event is also illustrated in Figures 7 and 9 from the vertical structure of the atmosphere seen in the soundings at Veracruz, Mexico located near the entrance of the gap (Figure 4). By 12Z 26 February, the cooler low-level air is confined by a strong inversion at about 690 hPa. Winds below the inversion at 690 hPa were predominantly out of the north and changed to westerly abruptly at the inversion. There was also a weak inversion and a dryer layer at about 870 hPa. The winds were weaker and veering under this weak inversion. This was suspected to merely be a result of local topographical effects and would not impact this outflow study.
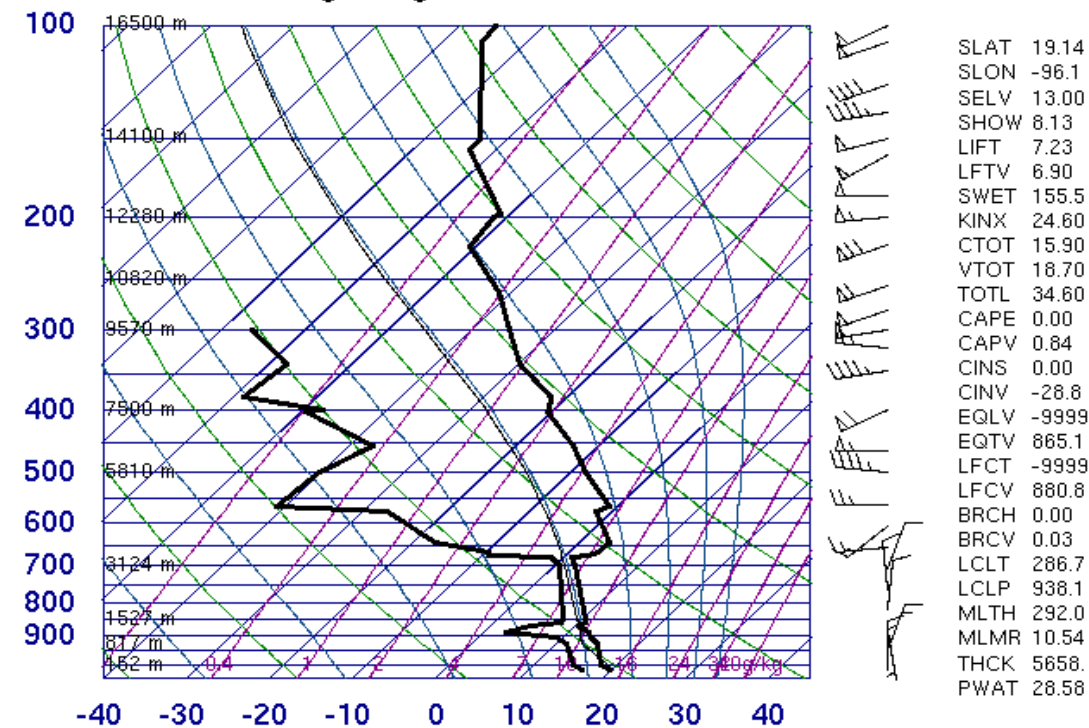
Figure 9.   Sounding near Veracruz at 12Z 26 February illustrating the postfrontal boundary layer northerly winds extending from the surface to 690 hPa and the winds backing abruptly to westerly above the strong inversion.

18

Visible satellite imagery was also analyzed to characterize the gap outflow development and track the progression of its leading edge. The leading edge was well marked by a rope cloud feature as indicated in Figure 10. As with the study by Steenburgh et al. (1998), this rope cloud will be used to draw isochrones of the leading edge. These isochrones will then be drawn over the COAMPS model output for comparison.
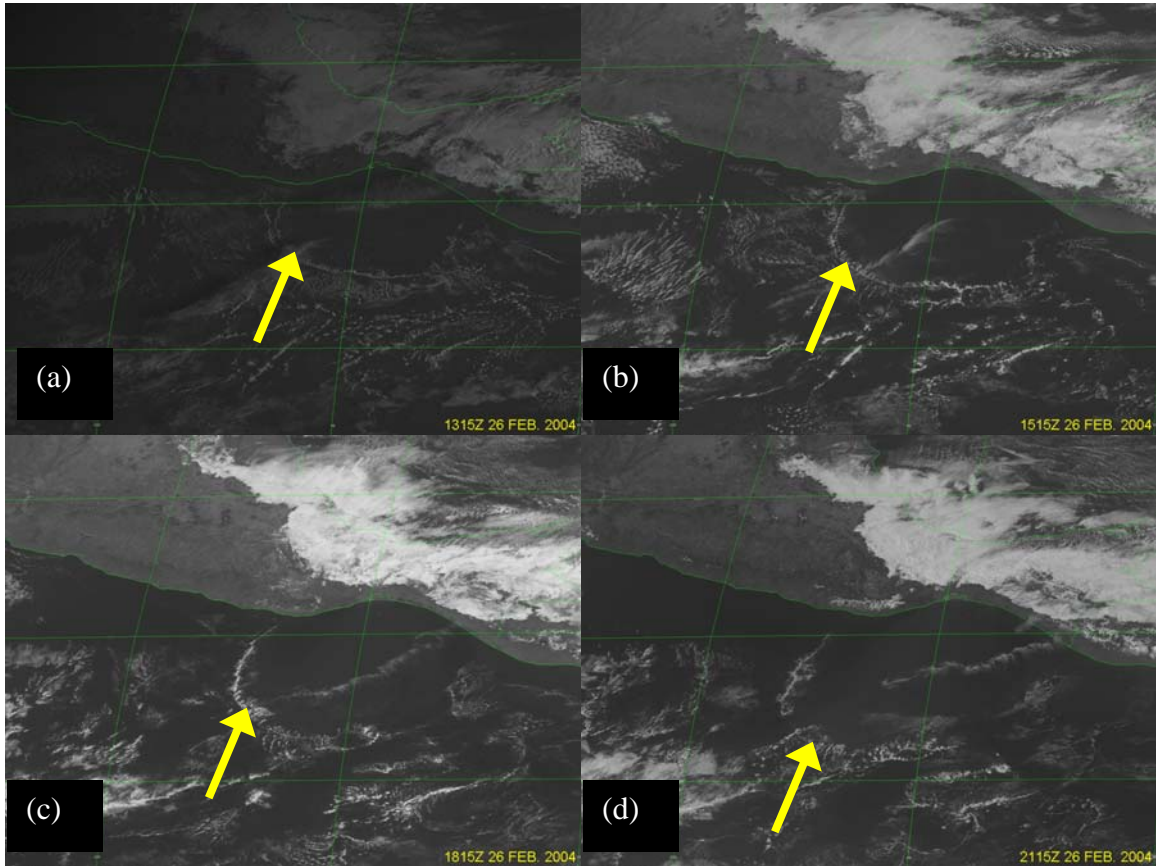
Figure 10.   Visible satellite imagery from GOES East for February 26 at (a) 1315Z, (b) 1515Z, (c) 1815Z, and (d) 2115Z. The yellow arrow is indicating the leading edge rope cloud of the gap outflow (after NOAA's Comprehensive Large Array-data Stewardship System at http://www.class.noaa.gov/nsaa/products/, last visited 18 September 2006).

Scatterometry wind measurements interpolated to 0.25 degree were plotted using MATLAB in Figure 11 for the approximate pass times of 01Z and 12Z 26 February and for 00Z 27 February. Figure 11a shows that the outflow had just exited the gap and was

pushing southward over the waters of the Gulf of Tehuantepec. Figure 11b missed the jet core development; however it does show a broad northwesterly flow south and east of the gap exit region.

Figure 11c at approximately 00Z 27 February shows the extent of the jet core very well. The jet core axis is seen to extend towards the southwest to about 12N 97.5W before reaching the edge of the scatterometry coverage. Maximum winds are closest to the coastal gap exit region, but due to near shore contamination, those maximum winds are not distinguishable in this figure. However, the trend of increasing winds towards the coast is observable to a maximum of about 17 m s^{-1} at about 15N 95W.
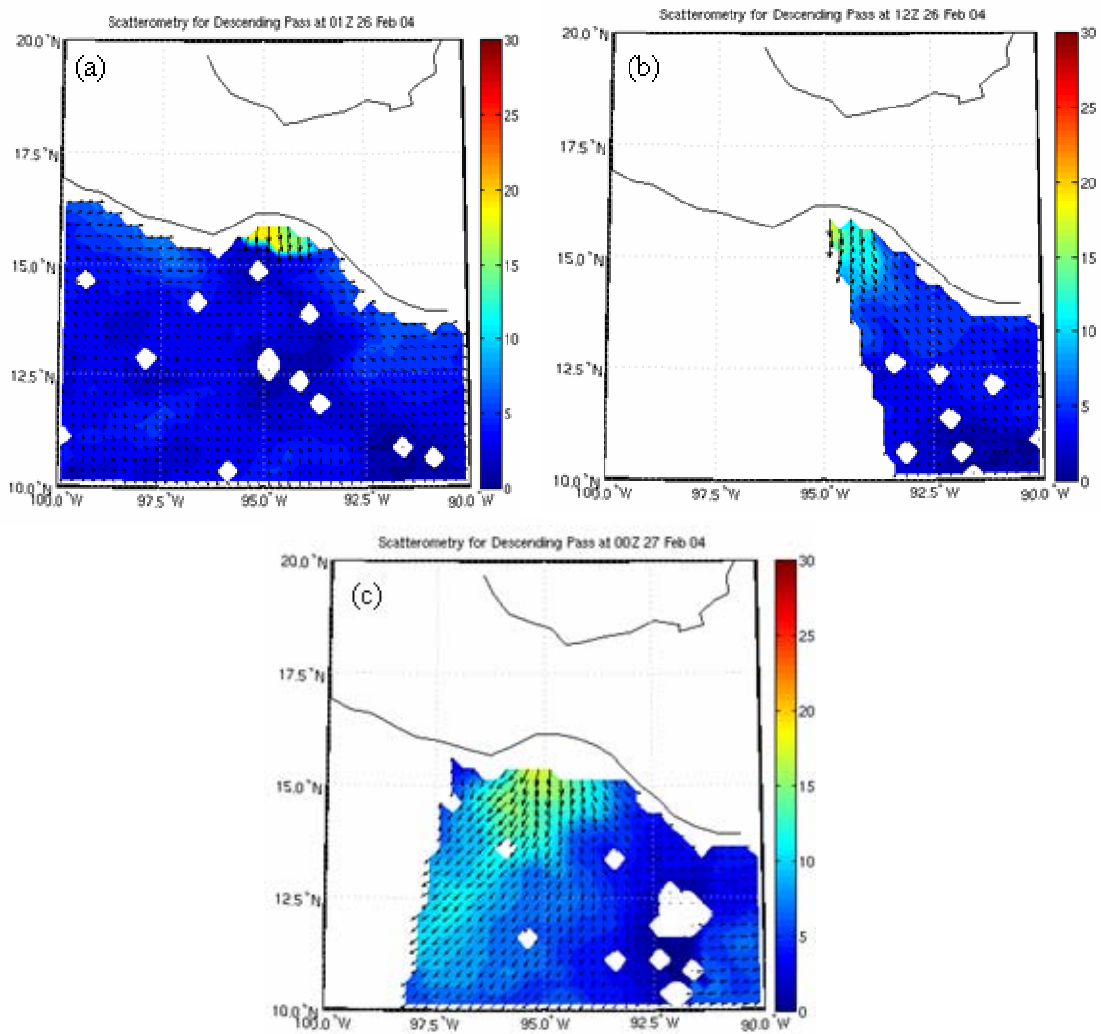
Figure 11.   Contoured scatterometry winds (m s^{-1}) over the Gulf of Tehuantepec at approximately (a) 01Z 26 February, (b) 12Z 26 February, and (c) 00Z 27 February. Vectors show direction of wind. The scatterometry data has 0.25 degree resolution.

IV.   ANALYSIS OF COAMPS MODEL RESULTS

A.   COAMPS MODEL SETUP AND INITIALIZATION

The COAMPS simulation for GAP022504 was initiated at 00Z 25 February and continued to 12Z 27 February. The model was updated with new NOGAPS boundary conditions, data assimilation, and first guess field for a new initialization every 12 hours. For analyses presented in this thesis, we use the results from the run starting at 12Z 26 February, approximately 12 hours after the onset of the gap outflow.

The simulation showed considerable oscillations, especially in the pressure fields, for the first six hours of this run. The pressure was initially too high particularly in the southern portion of the inner-most domain. The model stabilized from this initial adjustment by about 18Z.

B.   COAMPS GAP-OUTFLOW CHARACTERISTICS

1.   Development of Gap Outflow Jet

Figure 12 is a four panel diagram showing wind speeds, contoured and color filled, along with vectors showing the wind direction of the 10 meter COAMPS wind field. The panels represent time increments of every three hours starting at 12Z 26 February. Also shown on the plots in Figure 12 is a yellow line that marks the location of the rope cloud as an indication of the leading edge as observed from visible satellite imagery. The 12Z image does not have the leading edge marked because the visible image was still dark at 12Z.

Figure 12 shows that at 12Z the event was already well developed and the outflow reached hundreds of kilometers offshore. The highest winds occurred just offshore directly downstream of Chivela Pass with winds peaking at about 22 m s^{-1}. This offshore maximum was also noted by Steenburgh et al. (1998) as discussed in Chapter I.

Another noticeable source of outflow is evident to the east of Chivela Pass as the rising terrain east of Chivela Pass gives way to another relative low in the coastal topography in the Mexican state of Chiapas. As with the Chivela outflow, maximum wind speeds at 10 meters were found just offshore and peaked at about 22 m s^{-1}. There

was no evidence to confirm the existence of this secondary outflow source. The scatterometry passes in Figure 11 showed a generally north-northwesterly flow along the coastal region southeast of the main gap outflow. Also, the aircraft did not fly through this secondary outflow to confirm its existence. However, since the scatterometry cannot determine the near coastal winds, due to coastal contamination, and no other data here directly disputes its existence, it cannot be completely discounted. The sounding at 12Z 26 February sounding at Veracruz (Figure 9) indicates that the dense air mass is capped by an inversion at about 3200 m which is far above the average 1500 m terrain in the state of Chiapas. It is apparent that the high resolution terrain of COAMPS is allowing the flow over the Sierra Madres of Chiapas and is representing another gap outflow at this location. This flow becomes weaker, however, as the model steps forward in time. These are the only major sources of outflow over the Gulf of Tehuantepec found in this simulation. It is notably different than the MM5 results found by Steenburgh et al. (1998) in that there are two distinct and separate sources rather than a single broad source of outflow. Between the two major jets was an axis of relative minimum winds which persisted throughout the period of this run.

Elsewhere along the coast, there appeared to be the expected diurnal cycle of land/sea breeze. At 12Z, a land breeze was in effect along the entire Pacific coast with the exception of the enhanced wind near the outflow regions. This was evident since the coastal offshore winds were considerably different than the background synoptic forced northerly winds away from the coast. Alternatively, at 21Z, a sea breeze influenced the majority of the coast.

Away from the coast, the winds gradually weakened and fanned out, with a considerable increase in fanning out near the leading edge. The leading edge of the outflow was apparent as it was marked by a distinct line of flow convergence. As the flow fanned out, it formed two eddies on either side of the jet. To the west of the jet, an anti-cyclonic eddy formed. To the east of the jet, a cyclonic eddy formed. Also, as the leading edge progressed further offshore, so did the location of the eddies. This allowed a broader region of near coastal return flow. This is also apparent in the MM5 run, however, the cyclonic eddy was notably further offshore at the relative stages of the event and more defined throughout the event in the COAMPS run. By 21Z, both eddies were

undergoing weakening. The western eddy had become a broad region of weak anti-cyclonic flow and the eastern eddy had weaker near coastal return flow. This trend continued to 23Z.

Another noticeable feature is the wind maximum on the western most portion of the main Chivela outflow. This feature is persistent throughout the simulation period. In addition, upstream from this maximum, it appears that the air that feeds this maximum has flowed over the terrain just west of the Chivela Pass. The maximum is located just east of a near coastal terrain ridge (Figure 4).

The observed leading edge, marked by the yellow line, indicates that COAMPS did a poor job of simulating the southward and southeastward progression of the outflow. The maximum wind jet core appears to cross the 97.5W longitudinal line near 14N. This is almost two degrees north compared to that seen from the scatterometer winds at the same longitude. Also, the studies by Chelton et al. (2000), Steenburgh et al. (1998), Clarke (1988), among others, all indicate a more southward location of the outflow jet in conditions when large scale synoptic forcing are secondary to forcing from the local topography. Since GAP022504 was under similar weak synoptic forcing as described in Chapter III, the source of error for misrepresenting the southern outflow leading edge is likely in the model physics/numeric. We noticed the presence of local divergence at the simulated southern edge of the outflow, which are denoted by the red circles in Figure 12a at 12Z 26 February. Such divergence features at the leading edge disrupt the flow to the south and favor the formation of the cyclonic eddy to the east. However, in examining multiple gap events in the region using scatterometer wind, we have not confirmed the presence of similar divergence pattern. Further study is needed to identify the source of this divergence pattern and how it is related to the misrepresentation of the leading edge to the south.

The western progression of the leading edge, and the wind speeds associated with the outflow, matched that of the satellite imagery and aircraft wind data (discussed further in Chapter V) fairly well. Therefore, the remainder of this study will mostly focus on the areas of the model that were well representative of the conditions observed.

23
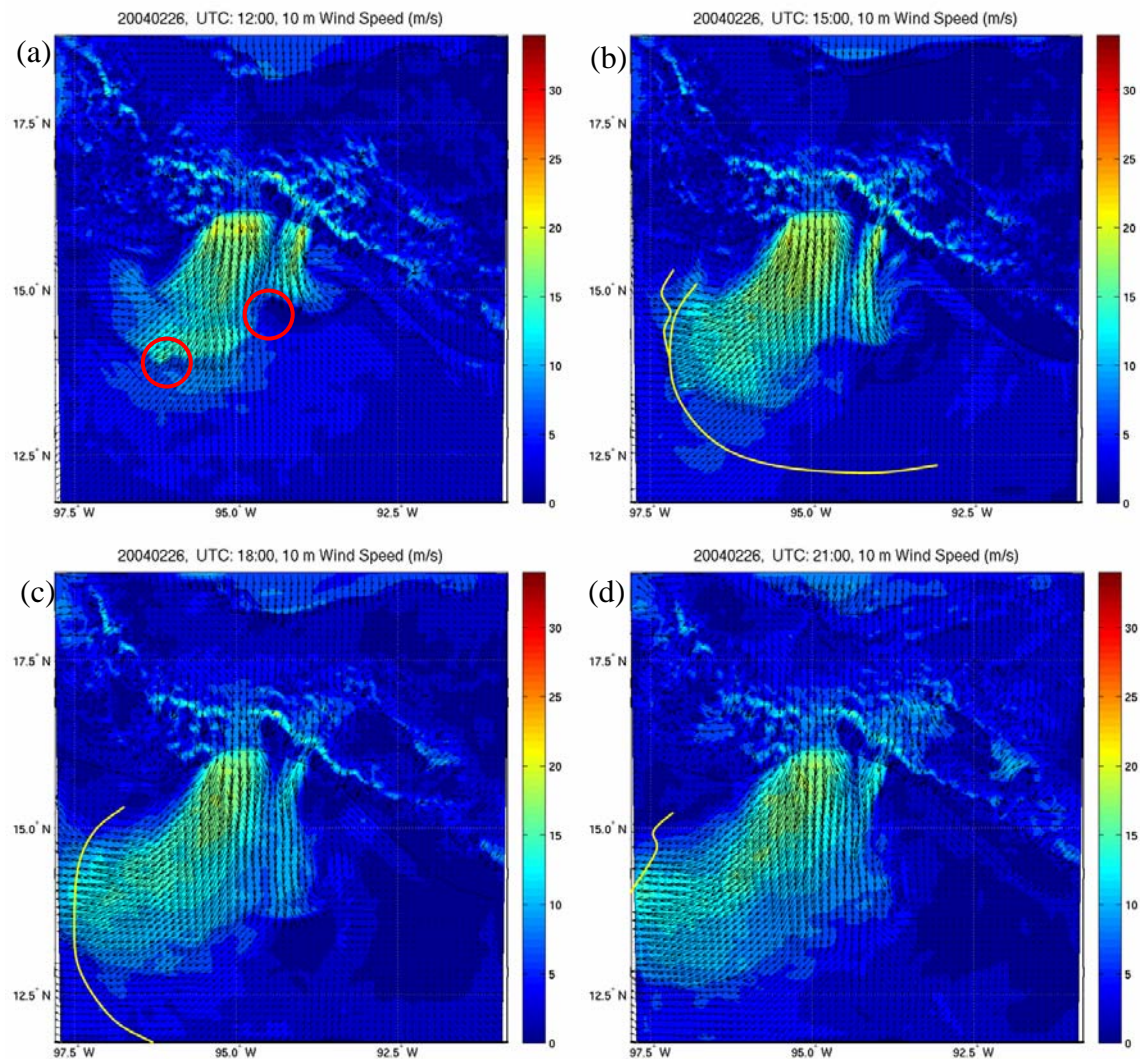
Figure 12.   COAMPS simulated wind speed contours in ms^{-1} and wind vectors at 10
m analyzed on 26 February at (a) 12Z, (b)15Z, (c)18Z, and (d) 21Z. The length of the
wind vector is proportional to its magnitude. The yellow lines indicate the leading edge
identified from satellite imagery. The red circles in (a) indicate locations of points of the
divergence pattern at initialization.

Figure 13 shows the development of the surface pressure during the gap event.
The lower limit on the color bar was set to mask out any contouring over the terrain as
the pressure at elevated terrain would be lower than 1010 hPa. Here, model adjustment
to initialization is most noticeable. During the first six hours of adjustment, oscillations
of surface pressure are observed to occur over the entire field, particularly larger near the
southern boundary where oscillations of 3 hPa were simulated in successive hours. The

outflow region of the model also showed pressure swings during the first six hours, however, it mostly stabilized by 18Z. The southern region continued oscillations by 1 to 2 hPa through 21Z.

Higher pressure was indicated near the gap exit throughout the run. This led downstream into a pressure ridge that appears to be located along the approximate location of the simulated jet axis. Local pressure minima exist on both sides of the jet axis and coincide with the anti-cyclonic and cyclonic eddy features. The cyclonic low pressure minimum was notably lower. By 18Z, the cyclonic eddy is still coincident with the eastern low pressure with return flow along the coast, but the western anti-cyclonic eddy is not coincident with the lowest pressure. Rather it corresponds with a trough axis. The pressure along the coast on the western side of the eddy is higher which accounts for the westerly return flow. There is a large pressure gradient on either side of the jet axis towards the corresponding eddies.

There also appears to be a pressure minimum along and just behind the leading edge of the outflow, most notably along the western leading edge. The pressure minimum follows along the leading edge towards the south around the fanlike shape of the outflow. This feature is most prominent early in the run; however, it is still observable at 18Z and later along the southern outflow boundary.

It is suggested here that due to initialization adjustments and an unrealized relative pressure ridge over the southern region of the domain early in the run, the outflow experienced an additional southerly pressure gradient that prematurely turned the outflow towards the west. The points of unnatural divergence (circled in Figure 12a) that existed early in the run along the southern leading edge may also have aided in the development of the strong cyclonic eddy feature modeled by COAMPS. After the model stabilized by about 21Z, the outflow pressure ridge began to align more with what was indicated by the scatterometry and previous studies, however, the flow had already been disrupted along with the southern progression of the leading edge.
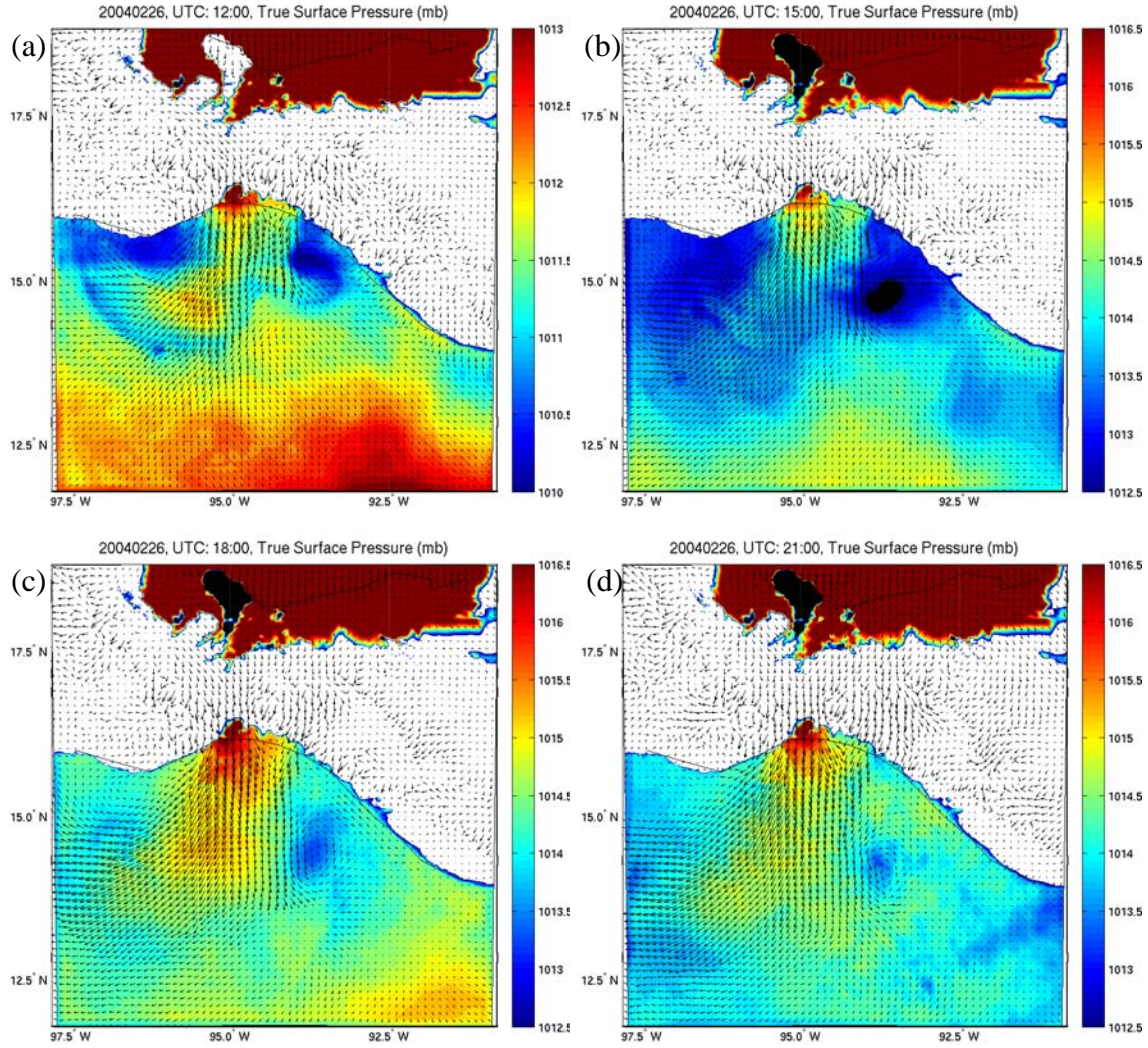
Figure 13.   Same as Figure 12, except for surface pressure in hPa.

2.   **Thermodynamic Characteristics**

Figure 14 shows the potential temperature at 10 m. The tongue of cold air from the outflow is apparent through 18Z and seems to be aligned with the path of the outflow. After 18Z, however, the temperatures begin to warm considerably and the cool tongue of air is no longer as profound. Also, within the secondary outflow from the state of Chiapas, the cool air signature only faintly remained by 18Z and by 21Z, the secondary outflow actually has become a source of higher potential temperatures. The daytime heating of the terrain is the likely reason of this evolution. This will be discussed further later when the sensible heat flux variation is analyzed.

On a larger scale, warm air also appears to narrow and warm the cool air tongue of the Chivela outflow as the model run progresses. Early in the run on both sides of the jet, markedly warmer potential temperatures exist separated from the outflow. Later, however, the edges of the outflow itself show much higher potential temperatures.

The cool tongue of the jet is surrounded by warm air in the coastal region. As seen in the water vapor distribution (see Figure 16), the warm surroundings are also low in moisture. Apparently, the warm and dry surroundings are limited to the coastal region and associated with northerly flow. It is likely associated with the effect of the mountain range where subsidence in the leeside of the mountain range produces warmer and drier air. Another influence could be the advection over warm coastal SST (Figure 15). Further investigation is needed to determine the origin of the coastal warm band. This warm band, however, appears to be advected along with the leading edge. A contribution to the warm band may also be due to a secondary direct circulation that COAMPS models ahead of the leading edge. This is discussed further in Chapter V.

The eddy circulations also appeared to have warmer potential temperature associated with them due to the return flow of coastal warmer air. The anti-cyclonic eddy was slightly cooler, however, which could be due to its proximity to the coastal land breeze from 12Z to 15Z whereas the cyclonic eddy initialized further offshore and moved even more offshore. In addition, relatively cool outflow seemed to already be entrained into the anti-cyclonic eddy.

The position of the anti-cyclonic eddy moved relatively little until after 18Z when it became more elongated. The center then moved towards exiting the domain by 22Z. The reason for the residence time of the anti-cyclonic eddy is due to the outflow following its inertial path around the region of the anti-cyclone, effectively holding it in place until the leading edge continued far enough west that it became elongated.
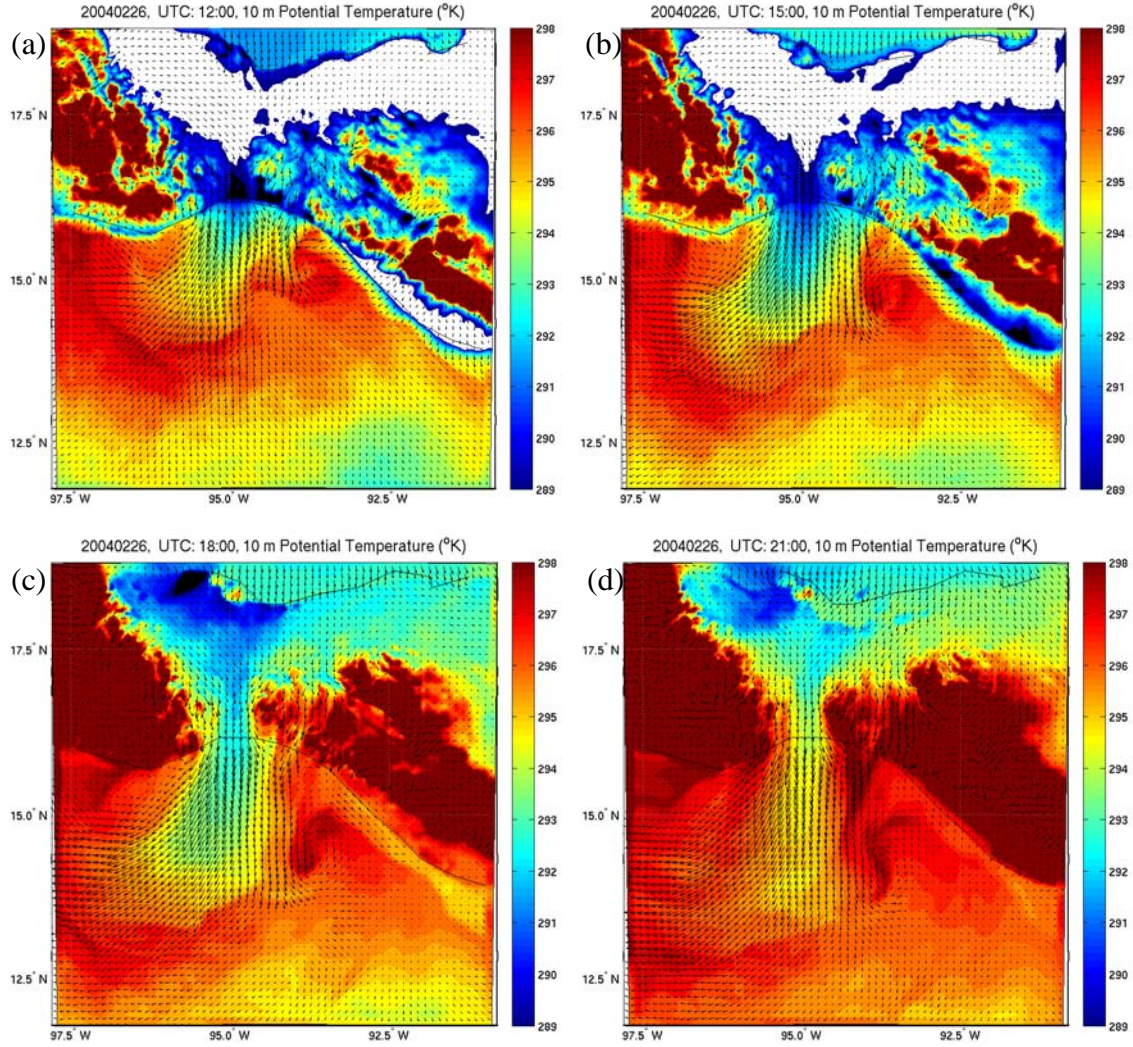
Figure 14.   Same as Figure 12, except for potential temperature in Kelvin.

The SST for the 12Z 26 February COAMPS run is shown in Figure 15a. The black lines indicate the aircraft low-level flight tracks for comparison later. The SST field was only updated with each new run every 12 hours, therefore this SST representation was constant throughout the 12Z 26 February model run. This constant SST field for 12 hours could be a reason for discrepancies between the observed and modeled surface fluxes (Chapter V) through static stability and boundary layer mixing. The SST field for 12Z 27 February is also shown in Figure 15b. The difference between the two SST shows the time evolution of the SST field over the 24 hour period as seen by the model.

Figure 15 shows the warmest waters are located coastally both to east of the outflow region near the Mexico/Guadalupe border and to the west of the outflow. Of interest is how the coldest SSTs are along an axis oriented NNW to SSE and not necessarily over the region with the maximum winds. The study by Clarke (1988) showed that the cold SSTs extended along the inertial path of the outflow immediately following a Tehuano event due to mixing and entrainment of the colder waters below the ocean surface layer and thinning of the ocean surface layer thickness due to the divergence caused by the Eckman transport properties. This is clearly not the case with the COAMPS SST field.

It is then observed that there is a local maximum in SST located at about 14N 96.5W. This maximum is located along the flight path of the research aircraft. The source for this maximum region is suggested to have formed from previous Tehuano events and the ocean response it produces. As Clarke (1988) discussed, the Ekman transport will push water to the right of the atmospheric forcing and therefore deepen the ocean surface layer by piling water to the right of the flow. Clarke showed that an anti-cyclonic eddy feature forms to the right of the Tehuano outflow on a scale that is similar to the inertial path expected by the outflow. This large warm eddy ocean response remains after the impulse forcing has diminished. Also, strong currents from the several day impulse wind forcing produces instabilities in the surface currents which can further complicate the ocean response. During the week following the previous Tehuano event, which occurred from 17 to 19 February, mesoscale ocean processes had adjusted the SST distribution to what is represented by the analysis in Figure 15a.
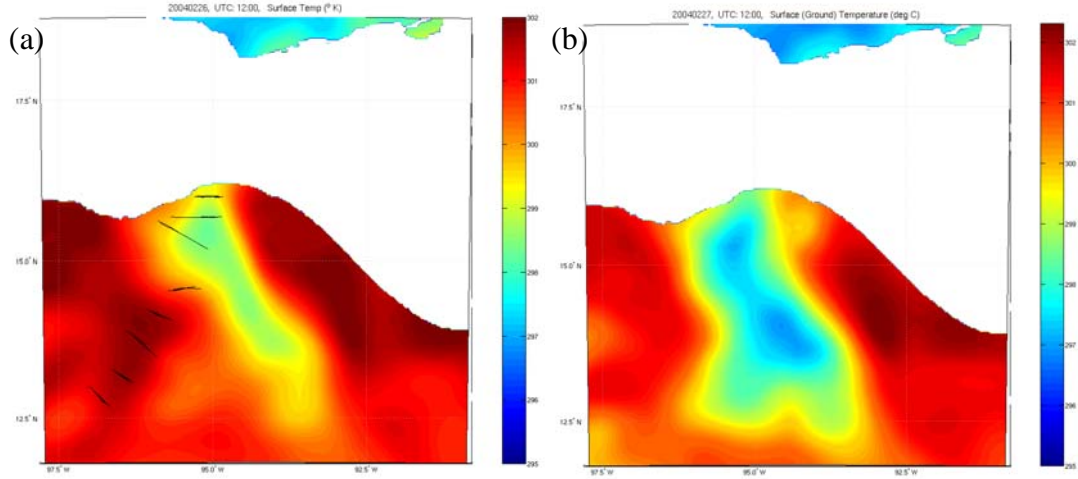
Figure 15.   COAMPS SST at (a) 12Z February 26 2004 and (b) 00Z February 27 2004. The black transverse lines indicate the position of the low level flight passes by the aircraft.

Figure 16 shows the evolution of mixing ratio (in g kg^{-1}) at 10 m above the surface every three hours. We observed that the highest moisture content is located behind the leading edge and throughout the entire outflow region. This is the case throughout the gap wind event. It appears that the lowest layer is picking up significant moisture as soon as the flow overruns water. Although it has lower potential temperature, it has picked up more moisture than the air ahead of the leading edge due to the higher winds providing for a large moisture flux to the atmosphere in the outflow region.

Another thing to note is the higher mixing ratios simulated along the coastal regions to the west and to the south. These appear to be the result of the nighttime land breeze that took place, with the moderate offshore winds picking up moisture after overrunning the ocean surface. This higher moisture coastal air can be seen wrapping into the eddy circulations.

The maximum mixing ratios are found to flow through the center of the gap over the lowest terrain of the Chivela pass. The air that is feeding into the western Chivela wind maximum is drier. Starting at 17Z, a dry slot is observed to source from the

30

western Chivela outflow and advect downstream. This appears to be a fluctuation in the model and may not have been realized nor can it be confirmed.
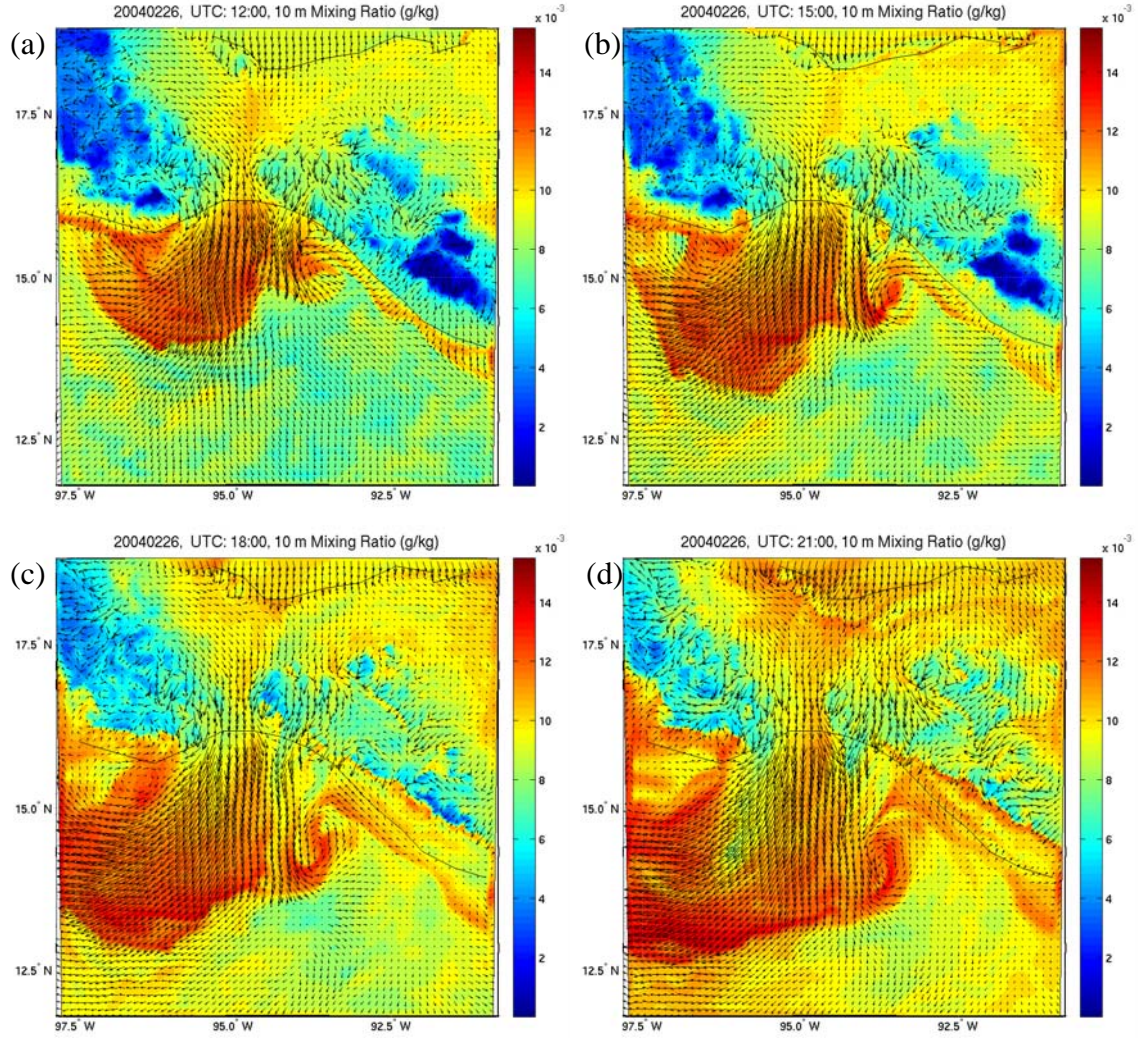
Figure 16.   Same as Figure 12, except for mixing ratio in g kg^{-1}.

3.   Air-Sea Fluxes

Surface wind stress is shown in Figure 17. This plot mirrors fairly well the wind speed variation discussed earlier. Noting again here that there are wind stress minima located in the regions of the eddies, as well as along the axis of convergence between the two modeled outflow sources.
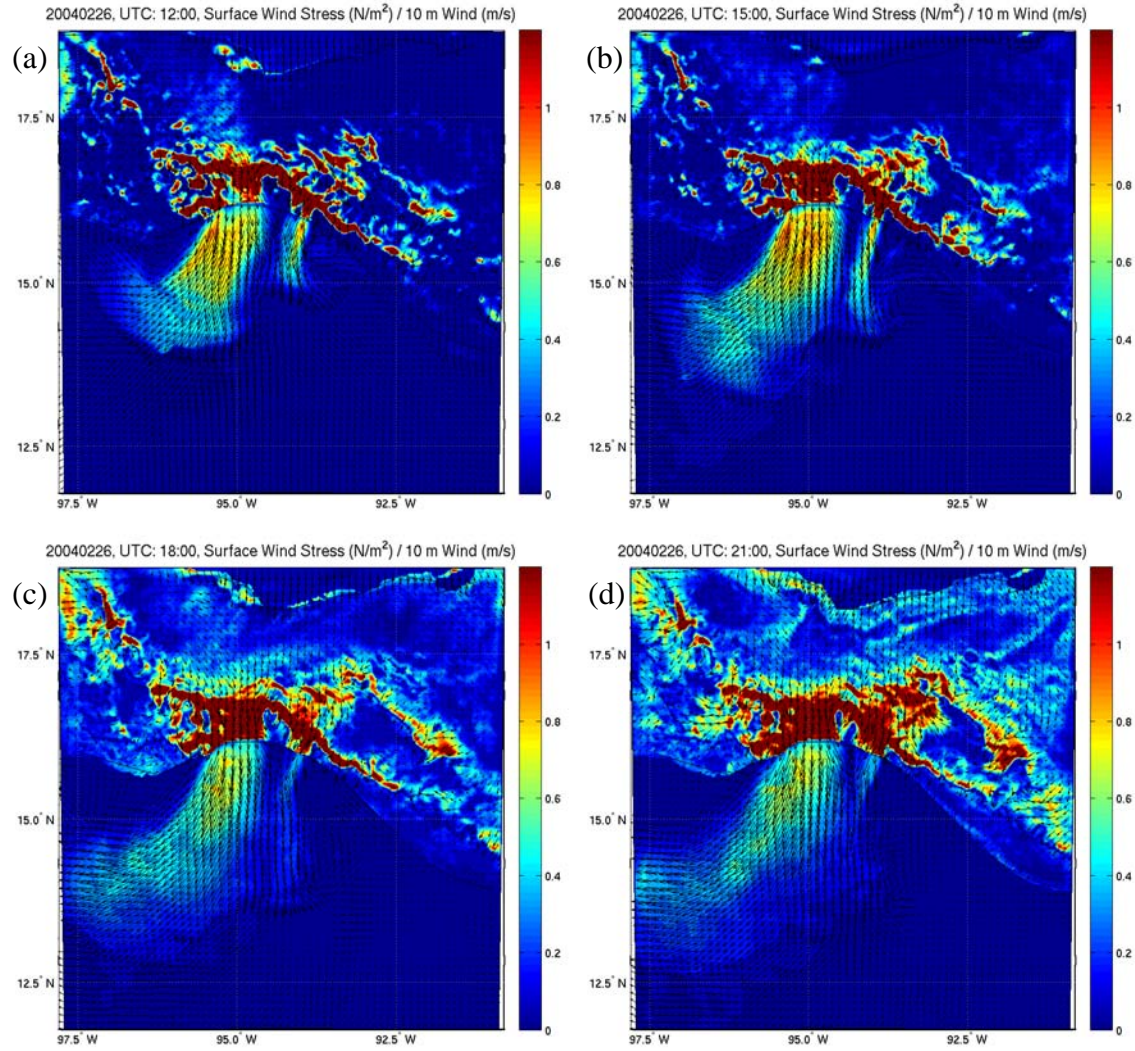
Figure 17.   Same as Figure 12, except for surface wind stress in N m^{-2}.

Figure 18 shows the sensible heat flux. Sensible heat flux is a function of both wind speed and the difference between the SST and the air temperature. Early in the run the sensible heat transfer to the atmosphere is at its highest since the air-sea temperature difference is also at its greatest for this 12 hour period. The highest values are found just off the coast immediately downstream of the two major outflows. It is also apparent that the nighttime ground temperatures are colder than the air temperatures since the sensible heat flux to the atmosphere is negative over land. Adversely, the effects of daytime heating are also represented. This is indicated by the sensible heat flux over land becoming largely positive by 18Z (Figure 18c). Since the air over ground is heated before advecting offshore, the sensible heat flux from the sea surface is greatly reduced.

After 18Z, a relative minimum in surface heat flux is apparent along the jet. The local maximum located farther downstream is due to the location of the warm SST anomaly near 14N 16.5W (Figure 15). The colder region of SST has a significant effect and the void of strong sensible heat flux is apparent. However, notice should be taken of the model simulation of positive heat flux to the atmosphere over all the water regions in this domain. This implies unstable surface layer stratification throughout the entire outflow region.

Also apparent is the positive near shore heat flux southeast of the gap flow that is a result of the nighttime land breeze between 12Z and 15Z.
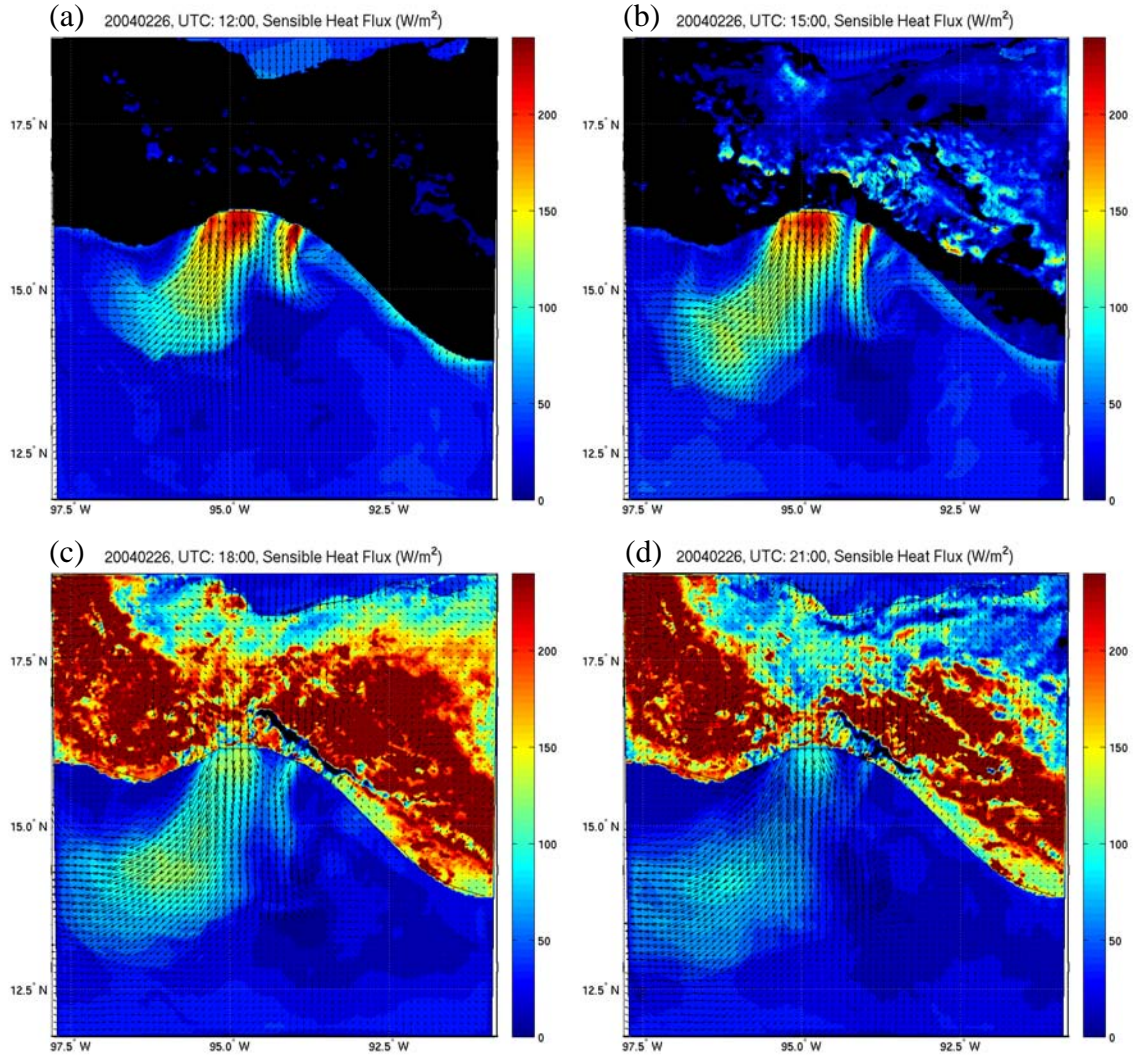
Figure 18.   Same as Figure 12, except for sensible heat flux in W m^{-2}.

The four time steps for latent heat flux are shown in Figure 19. The maximum latent heat flux occurs coincident with where there is dry air combined with strong wind imparted on the warmer waters. The higher latent heat flux along the coast due to the land breeze is visible at 12Z and 15Z. This flux also supports the relatively high mixing ratio near the coast.

More significant, though, is the large moisture flux immediately offshore of the outflow region that extends throughout the entire region affected by the outflow to just behind the leading edge. There is also significantly larger latent heat flux to the atmosphere along the western boundary of the Chivela outflow compared to the rest of the outflow. This feature coincides with the drier air descending from higher terrain noted previously that is feeding the western side of Chivela Pass (Figure 16). Also the secondary Chiapas outflow is drier and is seen to produce a much larger latent heat flux.

Another feature about the latent heat flux is the apparent local maximum located near 14.5N 95.7W. This feature coincides with the location of the significant SST gradient as the flow moves over the warm eddy. Finally, the even larger local maximum seen at 21Z near the same location corresponds to the dry slot mentioned earlier moving over the same SST maximum.
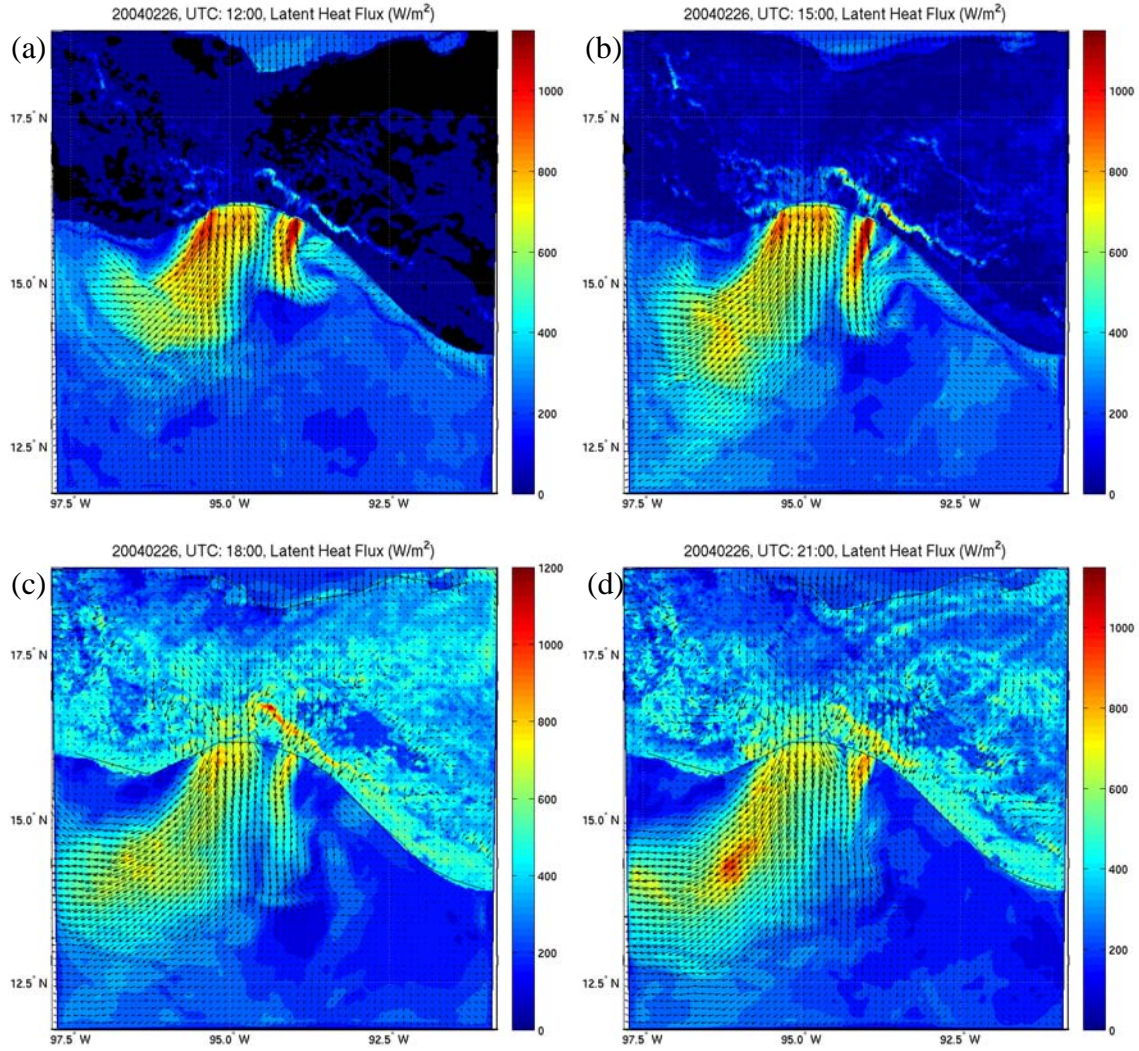
Figure 19.   Same as Figure 12, except for latent heat flux in W m^{-2}.

4.   Simulated Vertical Structure

a.   *Along the Jet Core*

In this section, we will use the vertical cross section to discuss the boundary layer structure in the outflow region simulated by COAMPS. Several cross section plots were created using the COAMPS model fields in order to examine the simulated vertical structure. The cross section, as indicated in Figure 20 (known as cross section 3, hereafter XSECT3), shows a cross section along the jet axis as simulated by COAMPS. The 15Z results were chosen so that this cross section could capture the leading edge structure before the leading edge exited the model domain to the west.

Figure 21 shows a four-panel layout for XSECT3 to include potential temperature, horizontal wind speed, mixing ratio, and vertical velocity. The vertical axis is in meters above the surface and the horizontal axis is in units of km along the cross section starting at point A (hereafter the reference point).

A quick glance at Figure 21 suggests that XSECT3 has two distinctly different regimes within the outflow, one from point A to 200 km down the jet axis (approximately the location of point C), the other between 200 km and 360 km, and then a third regime exists beyond 360 km out ahead of the outflow. Clearly, the leading edge of the outflow is around 360 km from the reference point as indicated by the abrupt decrease of wind speed (Figure 21b) and water vapor (Figure 21c). The leading edge is also characterized by a narrow region of strong upward motion with a maximum vertical velocity of about 0.7 m s^{-1} (Figure 21d), presumably a result of horizontal convergence at the leading edge as discussed in the previous sections. By examining the leading edge movements from 13Z to 16Z, it was found that the leading edge moved at a speed of 30 km hr^{-1}, comparable to that estimated from the position of the rope cloud identified in visible images.

The first regime between Point A and 200 km away is characterized by the presence of a jet in the capping inversion of the boundary layer. The jet maximum reaches nearly 30 m s^{-1}. The boundary layer is unstable between A and 10 to 20 km beyond point B and becomes well mixed after (Figure 21a), while a vertical gradient of water vapor exists in this regime, especially close to point A (Figure 21c). The strongest turbulence is also found within this regime with the maximum located near the coast (Figure 22).

A sudden jump of the boundary layer height at the beginning of the second regime can be identified clearly from potential temperature (Figure 21a) and water vapor (Figure 21c). Here, the boundary layer jumped from 500 m to about 1100 m over several kilometers. Accompanied with the jump are the abrupt decrease of wind speed and the disappearance of the low-level jet. These characteristics indicate that the sudden increase of the boundary layer height is likely linked to a hydraulic jump (Baines 1995).

To understand the nature of the inversion jump at point C, we calculated the Froude number before and after point C.

$$F_r = \frac{V}{(g'D)^{1/2}}, \qquad g' = \frac{\Delta\theta}{\bar{\theta}} g$$

where V is the boundary layer wind speed, D is the boundary layer depth, g is gravity (9.8 m s^{-2}), $\Delta\theta$ is the potential temperature difference across inversion base, and $\bar{\theta}$ is the mean boundary layer potential temperature. For regime 1, $V = 22$ ms^{-1}, $D = 500$ m, $\Delta\theta = 4$ K, we then have a Froude number of $Fr_1 = 2.65$. For the first 20 km of regime 2, $V = 15$ ms^{-1}, $D = 1100$ m, and $\Delta\theta = 4.5$ K, we then have a Froude number of $Fr_2 = 0.35$. Regime 1 is hence supercritical and regime 2 is subcritical, which confirms that the boundary layer height change at point C is indeed a hydraulic jump.

It should be noted that the location of the hydraulic jump moves away from shore following the leading edge of the outflow. From the simulations between 13Z and 16Z, it was found that the hydraulic jump is about 150 –210 km behind the leading edge. This is not surprising as the leading edge dynamics affect the wind speed variation as well as the inversion strength. In fact, regime 2 shows the largest variation of the boundary layer height where there is a large dip of several hundred meters near point D (Figure 21a) that shows more clearly in water vapor (Figure 21c). The presence of this dip is also seen at other times of the simulation. Figure 21d shows downward motion between points C and D with a smaller magnitude compared to that of the upward motion at the leading edge. This downward motion apparently resulted in the decrease of the boundary layer height behind the leading edge.

The divergence aloft over the leading edge also creates a weak jet in front of the leading edge as indicated in Figure 21b. This leading jet aloft tends to be drier than the air behind the leading edge in all the time steps after 13Z which suggests that it is out ahead of the cloud. Also, previous hours in the COAMPS simulation indicate strong downward motion within the boundary layer beneath the front end of this jet. This

suggests a secondary direct circulation is simulated out ahead of the leading edge. Again, no flight data exists in this study to confirm or deny that representation.
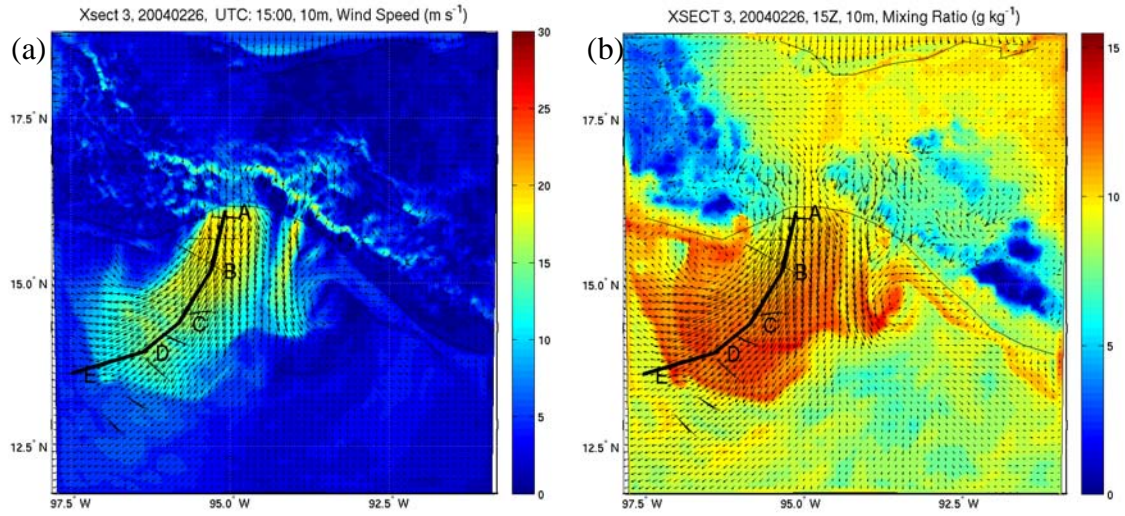
Figure 20.   Horizontal variations of (a) wind speed and (b) mixing ratio from 10 m height at hour 15Z of the COAMPS simulation. XSECT3 is marked by the dark bold line. The thin short segments are the aircraft cross jet low level flight paths.
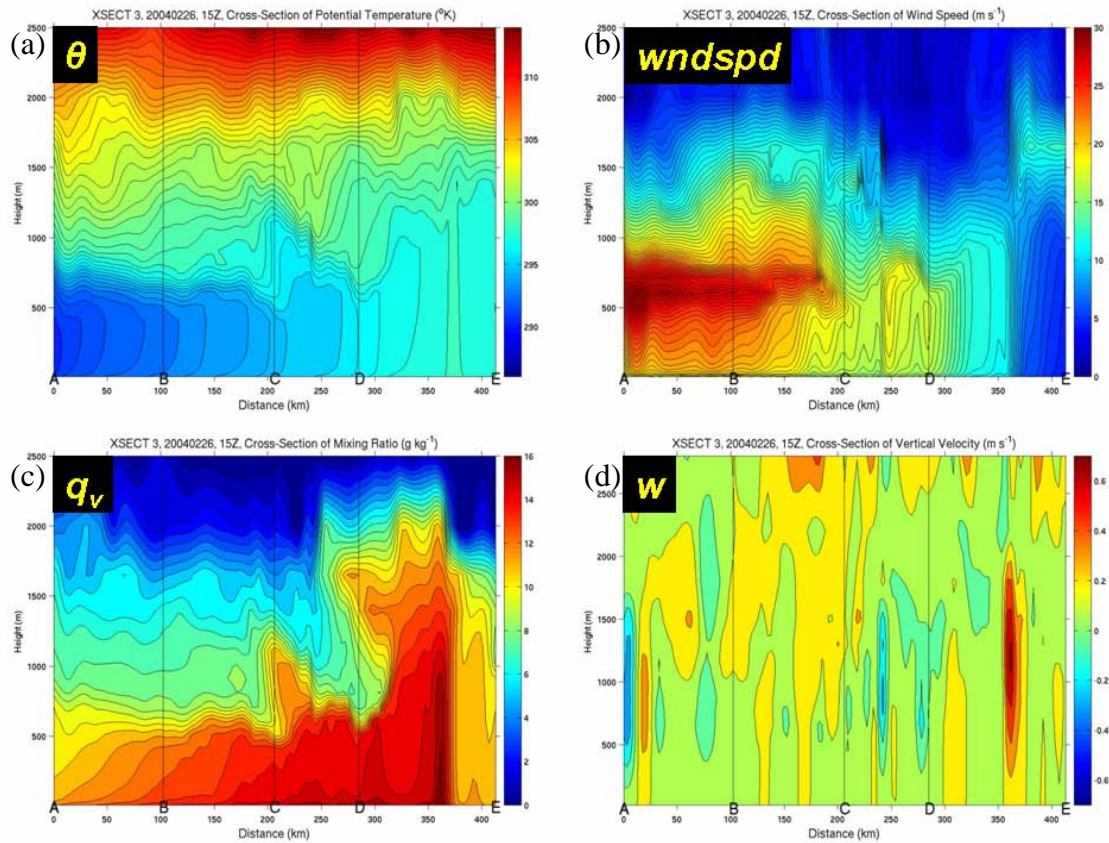
Figure 21.   Vertical thermodynamical structure along the outflow jet core (XSECT3).
(a) potential temperature, (b) wind speed, (c) mixing ration, and (d) vertical velocity.
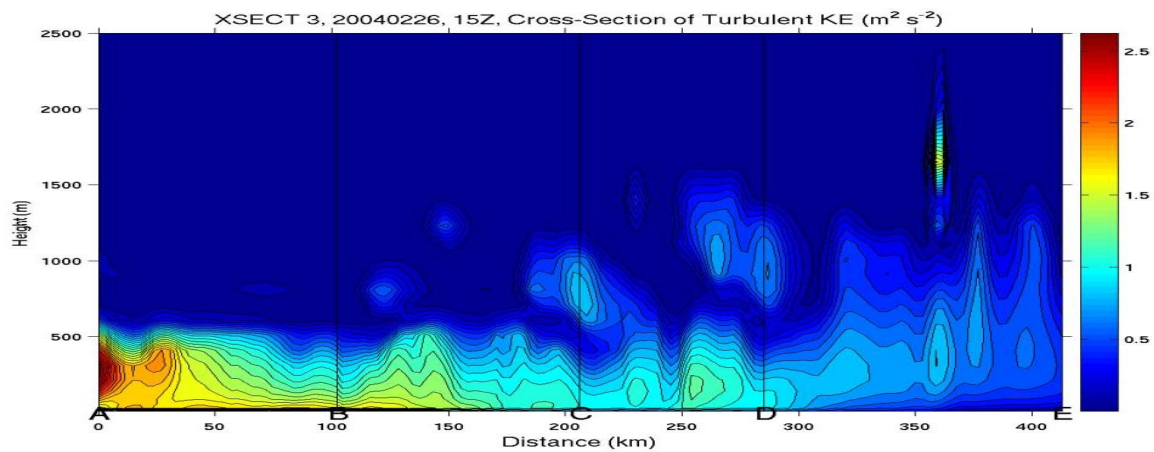
Figure 22.   Same as in Figure 21, except for turbulent kinetic energy.

39

b.   Cross Jet

Variations across the jet axis were also examined using cross section 1 (here after XSECT1) located nearest to the coast and gap outflow source (Figure 23). COAMPS results at 18 Z were chosen since the model had stabilized from model initial adjustment by that hour.

Figure 24 shows a four panel layout for XSECT1 to include potential temperature, wind speed, mixing ratio, and turbulent kinetic energy. The potential temperature plot (Figure 24a) clearly shows the colder temperatures in the jet core. The cold jet core also has the lowest boundary layer heights of about 300 m compared to its surroundings due to the downward vertical motion noted at and down stream of the Chivela Pass in the outflow.

The wind speed plot again shows the strongest winds above the boundary layer. It is also apparent that the core of higher wind speeds extends vertically to about 1500 m to 2000 m which corresponds to the elevation of the terrain on either side of the gap channel. Most notable is the very strong horizontal wind shear located at the western boundary of the outflow where the boundary layer jump is located. This suggests, as horizontal plots established earlier, that the boundary layer of the outflow to the west of the jet core did not originate from the same source as that in the jet core. The source for the boundary layer to the west is possibly composed of air that has either come from coastal region west of the gap or air whose trajectory has already gone completely around the anticylonic eddy to the west of the outflow and has been well modified.

The variation of the mixing ratio (Figure 24) also reaffirms the hypothesis of two different origins of the boundary layer on the west side. The large water vapor to the west of the wind shear and the vertical extension of those higher values is a product of the convergence created by the return flow on the north side of the anticyclonic eddy feature. It is not composed of the new outflow air from the gap undergoing a dynamic jump. The mixing ratio then shows a drop nearest point A. This is air found in the weak flow near the center of the anticyclonic circulation. The weak winds did not allow for significant moisture transfer to the air as will be discuss further in the next chapter.

The mixing ratio shows a thin and dry slot above the jet core. This feature was found to be a transient feature whose source and evolution was not deeply investigated. However, a quick look at the origin of this drier air seemed to be due to COAMPS modeling a dry air slot digging into the boundary layer air upstream of the gap. There was no data to verify the existence of this feature.

The turbulent kinetic energy plot shows strong mixing, as expected, in the vertically sheared environment near the surface below the jet core. It also shows some moderate turbulence west of the convergence zone in the well-mixed air of the anticylonic eddy.

Figure 25 shows the COAMPS surface values for air and sea surface temperature, wind stress, and sensible and latent heat fluxes along XSECT1. The wind stress and surface fluxes, as expected, show a similar trend. A sharp drop in wind stress west of the 150 km (not shown) and reflected by the small surface flux is further evidence that the boundary layer west of the shear is composed of different air than the outflow. Also apparent in Figure 25 is the surface pressure ridge along the jet core. Another characteristic of this COAMPS output of significance is the air-sea temperature difference. The air temperature is colder than the sea surface by about 2.5 to 5 degrees along the entire cross section. This will be discussed further in the next chapter when comparing these values to the aircraft data.
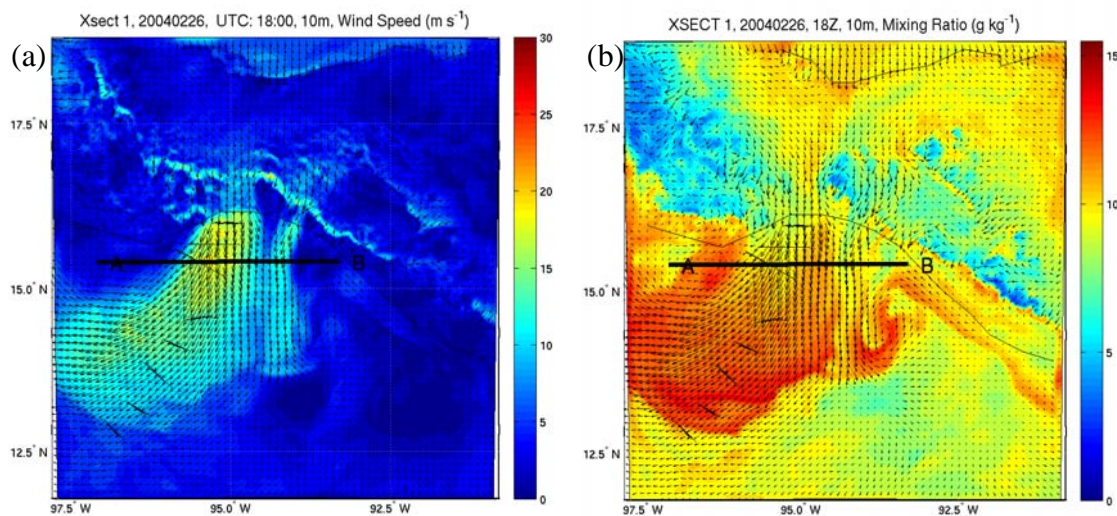
Figure 23.   Same as Figure 20 except for XSECT 1 at 18 Z.
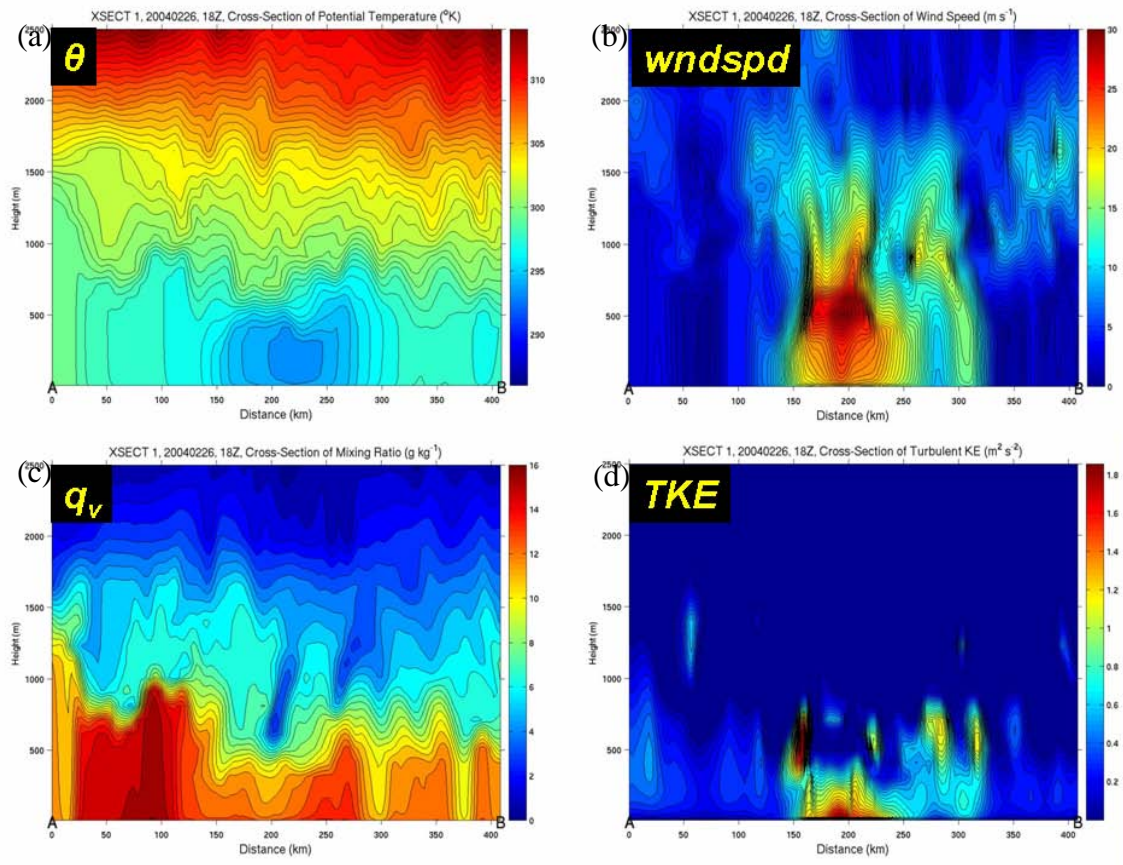
Figure 24.   XSECT 1 plots of COAMPS for (a) potential temperature, (b) wind speed, (c) mixing ratio, and (d) turbulent kinetic energy.
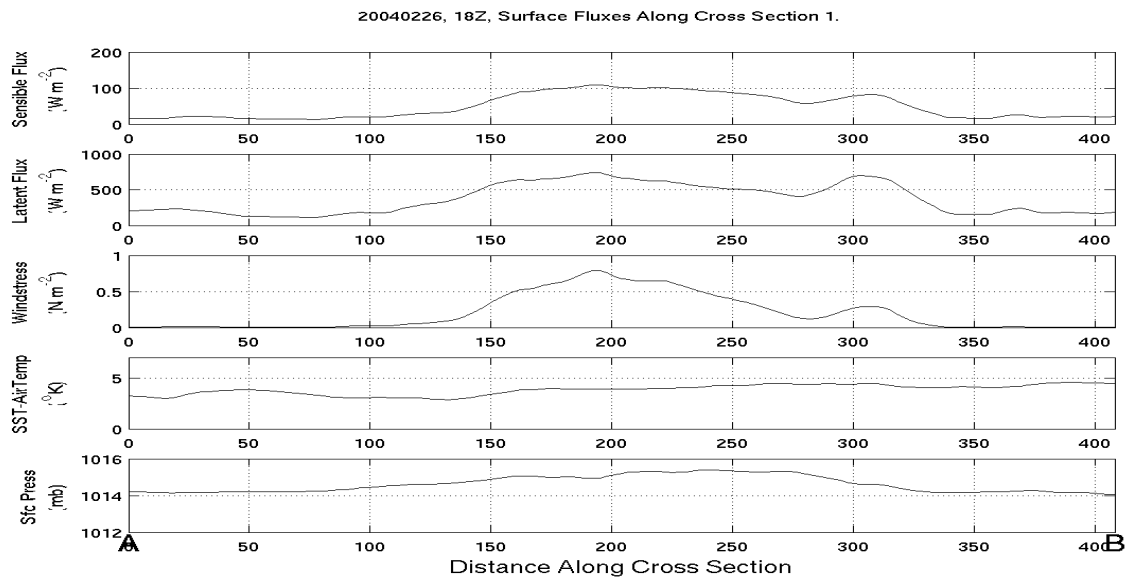
Figure 25.   COAMPS surface fluxes and surface values for XSECT 1.

V.   RESULTS FROM AIRCRAFT DATA AND COMPARISON WITH COAMPS MODEL

A.   AIRCRAFT FLIGHT PLAN

The NCAR C130 aircraft research flight number nine (RF09) was flown on February 26, 2004, began at about 14 Z and landed at about 22 Z from the nearby airport at Huatulco, Mexico. The flight plan was designed to take measurements along the predicted jet core axis making frequent cross jet low level legs. As shown in Figure 26, after takeoff the aircraft began its flight plan near the coast and worked its way south, then southwest. The aircraft did between one and four low level legs at about 40 m that were near normal the jet axis and then climbed to about 400 m to fly a leg of about 100 km downwind before then descending again to 40 meters and performing cross jet legs. After the aircraft had performed cross jet passes at seven different lines down the jet core, it then climbed to 1200m and made one continuous flight back upwind along the same path and dropped 14 dropsondes along the way. The aircraft then descended again to fly along the line it began at. This allowed for data at two different times over the same leg. The first leg was at 1452 Z and the repeated pass was about 6 hours later at 2117 Z. The aircraft then added another cross jet leg between the first two cross jet lines at about 15.7N before returning to land.

Due to the progression of the leading edge while the flight was underway, the aircraft was not able to fly through the leading edge.

In this study, several of the low level legs will be examined and compared against COAMPS. Specifically, Leg 1 and Leg 37 which overlap but at different times, Leg 7 which occurred in a stable environment, and Leg 22 which was downstream and in an unstable environment will also be discussed. The times of these legs were noted and the COAMPS model output was interpolated in time to match the time of the measurement.

Also in this study, the dropsondes will be analyzed and plotted against COAMPS output. The COAMPS results again will be interpolated in space and time to match the time and location of the dropsondes.

Finally, for this study, the vertical legs between the low level legs and the mid level legs allowed the aircraft to retrieve high spatial and temporal resolution data vertically from about 40 meters to 400 meters. This aircraft data will be examined for boundary layer processes that the dropsondes are unable to resolve.
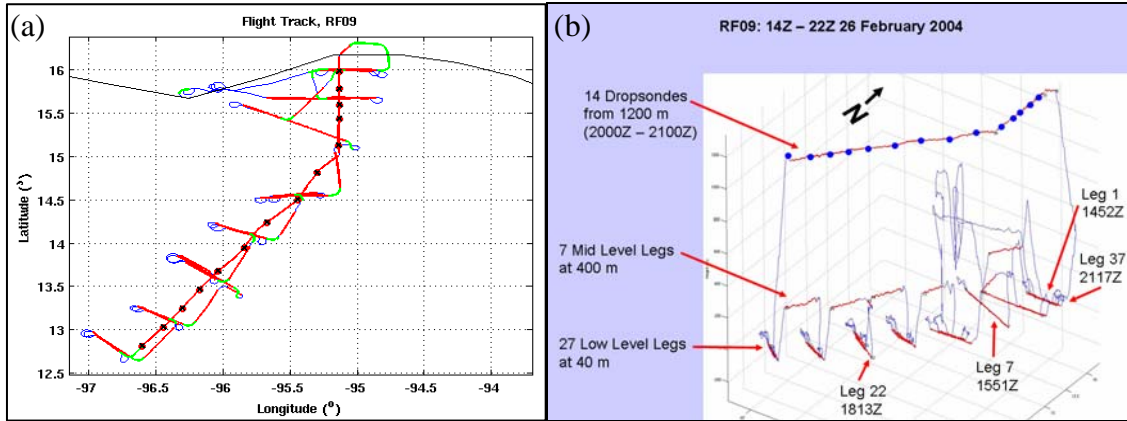
Figure 26.   NCAR C130 flight track for RF09 on February 26, 2004, showing (a) the overhead view and (b) an angled view. The solid black line in (a) denotes the coast line.

B.   DROPSONDE COMPARISON WITH COAMPS

The aircraft released and recorded data from 14 dropsondes along its flight path along the jet core axis between the hours of 20Z and 21Z. This leg of the flight, having taken less than an hour, can be considered to have ostensibly captured a snapshot of a cross section along the jet axis. The dropsonde data was plotted and contoured using MATLAB and is plotted in the left column of Figure 27. The right column of Figure 27 shows the corresponding data that was interpolated from the COAMPS output interpolated to match the time, location, and altitude of the dropsondes. The horizontal axis denotes the distance along the flight track from the dropsonde closest to the coast.

The vertical purple lines denote the range dropsonde data was recorded, which did not necessarily begin at the drop level of 1200 m. In addition, missing or bad data may occur for certain variables, such as water vapor.   In particular for water vapor, quality data from the dropsonde was only available below 800 m, which is the reason of smaller altitude range (Figure 27e) compared to other variables.

Contour plots of the wind speed (Figures 27a and b) reveal COAMPS' capability in predicting the general feature of the jet core. Both dropsonde and COAMPS show the

elevated jet close to the coast and the decrease of wind speed away from the coast. However, the dropsondes indicate a much stronger wind speed at its maximum as well as generally stronger winds throughout the entire dropsonde path. Also, the vertical wind shear is strong for both the dropsondes and the COAMPS model for the first 100 km, but the vertical wind shear in the COAMPS model diminishes significantly after that. COAMPS seems to produce comparable magnitude of the water vapor, but has much lower potential temperature above and below the boundary layer. In addition, the decease of the boundary height in the first 200 km and the increase of boundary layer height from 200 km to the end of the track are not depicted by COAMPS.

Because of strong spatial and temporal variations of the gap outflow, comparison directly between the observations and the model may be misleading at times. For example, if the model predicts a perfect spatial variation with, however, a time lag, direct comparison between model and observation at the same time and location may suggest poor performance of the model. This may be the case of the direct comparison shown in Figure 27. In order to understand what we are seeing, we attempted to find the relative location of the dropsondes relative to the true jet core. Figure 28 shows the aircraft observed wind speed and potential temperature from below 50 m height. It shows that the wind speed increases and the potential temperature decreases to the right side of each leg. Since the dropsonde track is approximately in the middle of the level legs, we therefore conclude that the dropsonde measurements were made on the left side of the jet core.

Figure 29 shows the wind speed and mixing ratio plots for 20Z around the time of the dropsondes. This figure shows that the dropsonde locations are near the COAMPS predicted jet core in the northern part of the flight track and are away from the jet as the jet turned to southwest. In fact, the dropsondes that occurred at the farthest southwest location were near what COAMPS was representing as the southern leading edge. In accordance to what was discussed earlier, the leading edge was actually much farther south and southwest by 20Z. Also, as compared to the scatterometry data, the jet was also farther south than what was represented by COAMPS. This deviation in the dropsonde track away from the predicted jet core may explain the larger differences seen in Figure 27 in the southern part of the track. On the other hand, the trajectory of XSECT

3 discussed in Chapter IV is closer to the predicted jet core at 20Z. We hence attempt to compare the COAMPS result from XSECT3 to those from the dropsonde (Figure 30).

Figure 27.   Contour plots of wind speed, potential temperature, and mixing ratio using MATLAB for (left column) the 14 dropsondes released by the NCAR C130 during RF09 and (right column) corresponding spatially and temporally interpolated COAMPS data.
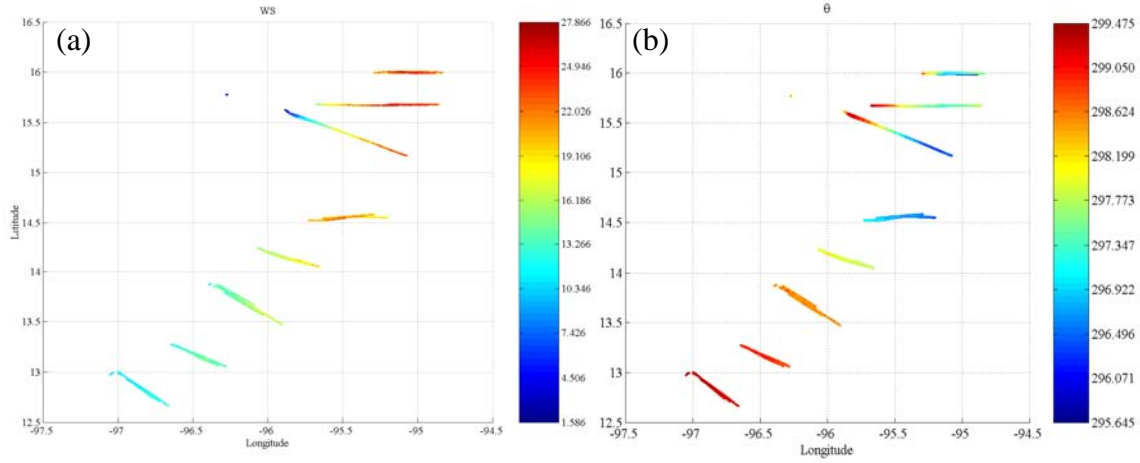
Figure 28. Spatial distribution of the aircraft measured (a) wind speed, and (b) potential temperature from below 50 m.
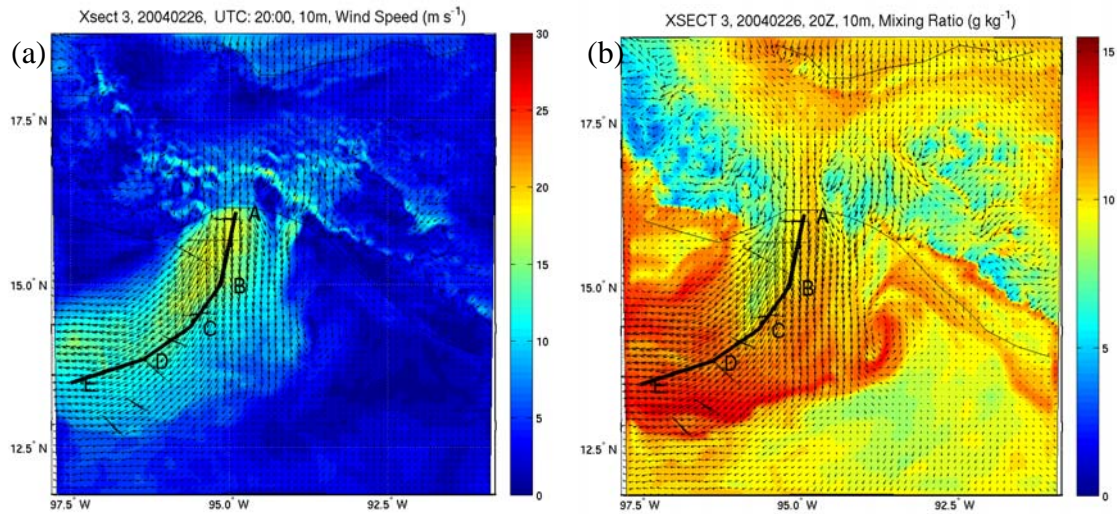
Figure 29. Horizontal plots of COAMPS (a) wind speed and (b) mixing ratio. Bold line denotes XSECT3.

Figure 30 shows that both the dropsondes and COAMPS results show a jet maximum that gradually decreases in height between 0 and 120 km down the trajectory. The height of the jet becomes relatively constant between 120 and 150 km and then gradually increases in height after about 150 km. Also, both plots indicate strong vertical shear in the boundary layer. However, a noticeable difference is that the jet is higher in the COAMPS cross section by about 200 to 300 m. Similarly, the potential temperature

47

and water vapor plots also indicate a higher boundary layer top in COAMPS (about 200 to 300 m higher). Further downstream, COAMPS shows a region of higher winds aloft at about the 200 km from the reference point whereas the dropsondes plot does not indicate these higher winds. However, observing that the dropsondes did not have data aloft between the 130 km and 250 km, this cannot be adequately compared. Beyond 250 km from the reference point, a very similar structural comparison continues in that there is a relative lull in the maximum winds at about 300 km, followed by another increase that seems to be much more vertically uniform below the 800 m height at about 340 km. Farther downstream, the winds again decrease remaining fairly vertically well mixed below 800 m.

The potential temperature plots also show a very similar trend along the cross section. The largest noticeable difference between the two is that COAMPS is between 2 and 5 degrees colder. COAMPS also shows a well mixed boundary layer, whereas the dropsondes indicate at least some stability, however weak, from the reference point to about the 200 km where the boundary layer top begins to increase with height again. While the dropsondes depicts a gradual increase of the boundary layer height beyond 200 km from the reference point, boundary layer top from COAMPS appear to increase in steps with significant variability although the general trend of boundary layer height increase is still seen.

The vertical stratification of water vapor is observed in both COAMPS and dropsonde results. The water vapor comparison also shows very similar structure noting again the lower boundary layer top for the dropsonde data. Also, the COAMPS simulation indicates much more significantly deeper boundary layer mixing at the 200 km mark, whereas the dropsondes, as with the potential temperature, show a gradual increase. Finally, the mixing ratio values are slightly higher in the COAMPS model.
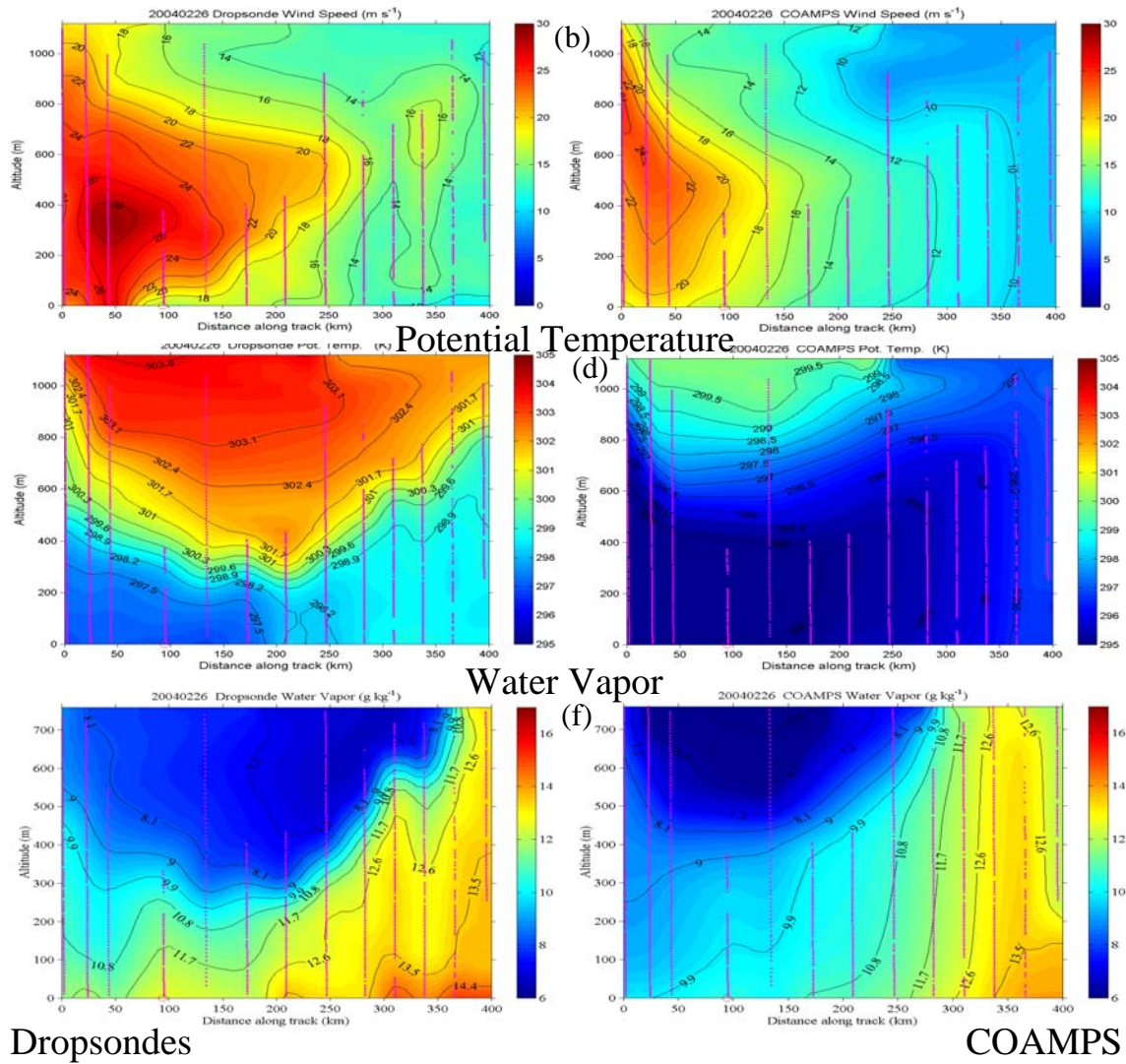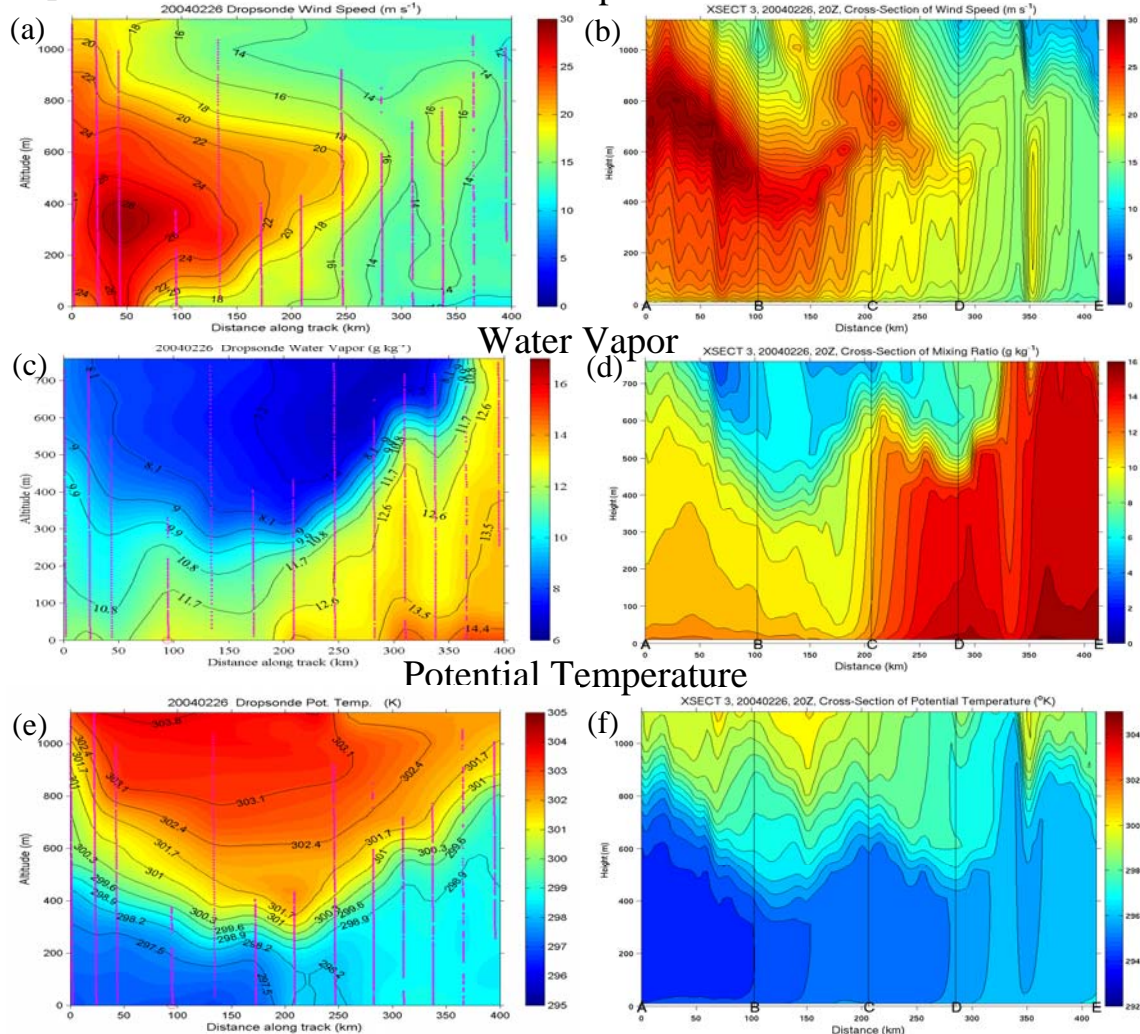
Figure 30. Contour plots of wind speed, potential temperature, and mixing ratio using MATLAB for (left column) the 14 dropsondes released by the NCAR C130 during RF09 and (right column) corresponding to the similar length along the COAMPS represented jet axis as represented by cross section 3 at 20 Z.

C. LOW LEVEL LEG COMPARISONS

We chose several low-level flight legs to compare between COAMPS and the observed quantities. These legs were selected as they represent different low-level thermal stratification: Legs 1 and 22 were made over unstable surface layer where the sea surface temperature is higher than that of the air. Leg 7 was in a stable surface layer where the coldest SST was found under the jet core. Leg 37 overlaps with Leg 1 except

that it was made 6 hours later. Comparisons between Legs 1 and 37 indicate the temporal change occurring during the event. Figure 31 shows where these legs are located and their orientation.
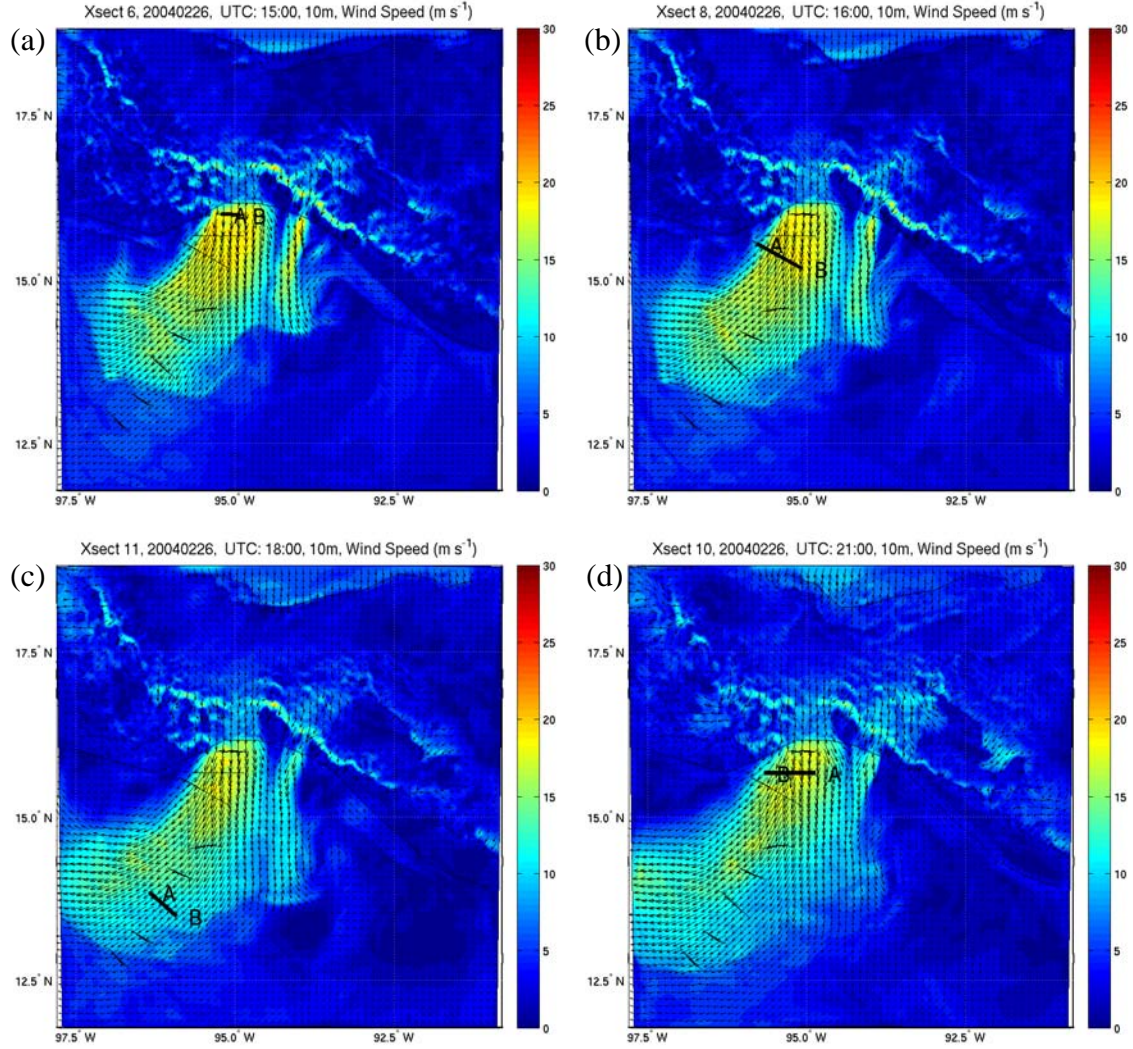
Figure 31. Location of C130 low level flight (a) Leg 1 at 1452Z, (b) Leg 7 at 1551Z, (c) Leg 22 at 1813Z, and (d) Leg 37 at 2117Z over laid on horizontal plots of COAMPS wind speed at the nearest corresponding hour to the leg time. Flight Leg 1 corresponds to cross section 6. Flight Leg 7 is cross section 8. Flight Leg 22 is cross section 11. Flight Leg 37 is cross section 10.

1. Unstable Conditions

Figure 32 shows the COAMPS-aircraft comparison in the observed unstable boundary layer. Here we find that the wind speed and direction are nearly perfectly

predicted while COAMPS potential temperatures were between 5 and 6 degrees colder than the aircraft measured temperatures. However, the decreasing trend towards the outflow axis was represented well. The sea surface temperature was, on average, warmer than the aircraft measurements by up to 1.5 K. This combination results in a sea-air temperature difference of above 7 K in COAMPS compared to about 1 K difference from observation. Hence, COAMPS is much more convective in this region. Consequently, the modeled sensible heat flux was significantly higher by an average 150 W m^{-2} over the magnitude calculated from the aircraft data (Figure 32).
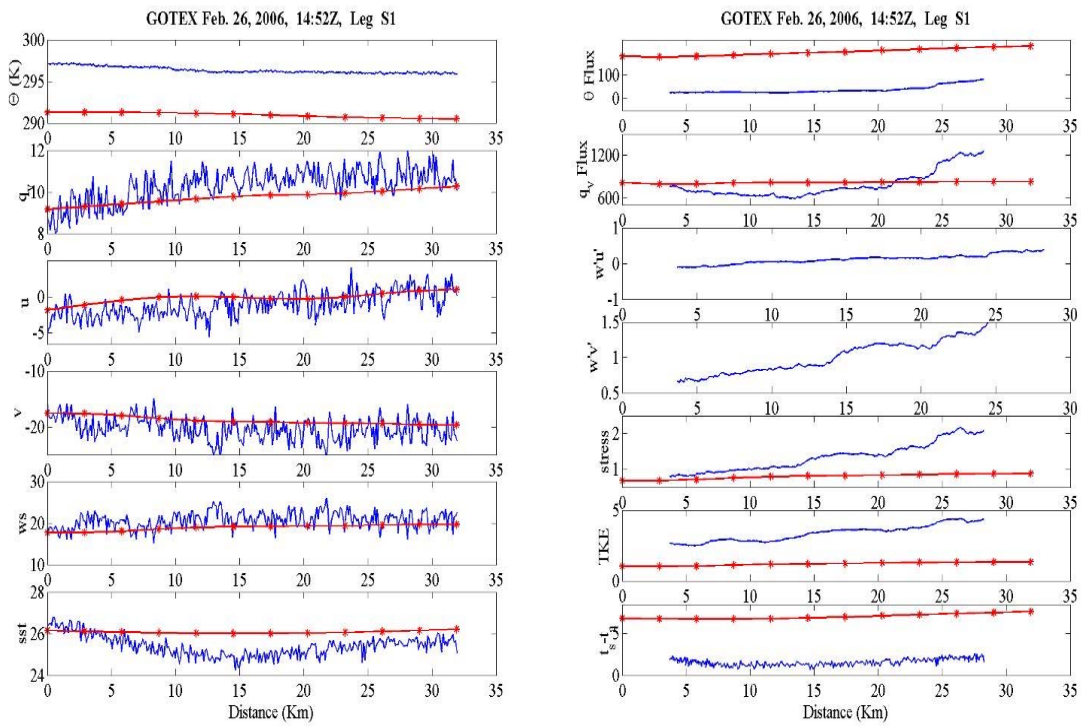
Figure 32.   Comparison between the aircraft measurements (blue line) and COAMPS results (red line) from RF09 Leg 1. The plots on the left from top to bottom are potential temperature (^{o}K), mixing ratio (g kg^{-1}), eastward wind component (m s^{-1}), northward wind component (m s^{-1}), wind speed (m s^{-1}), and sea surface temperature (^{o}C). The plots on the right from top to bottom are sensible heat flux (W m^2), latent heat flux (W m^2), eastward momentum flux (m^2 s^{-2}), northward momentum flux (m^2 s^{-2}), surface wind stress (N m^{-2}), turbulent kinetic energy (m^2 s^{-2}), and sea surface minus air temperature difference(^{o}C).

51

Although the wind components were well predicted by COAMPS, large deviation is seen in the surface stress towards the jet core, which indicate the inadequacy of the surface flux parameterization near the jet core. Similarly, the largest difference in latent heat flux is also seen at the location with significantly higher stress, although the mean water vapor differs only slightly. Turbulent kinetic energy was also significantly under predicted by COAMPS.

Figure 33 shows the comparisons between the aircraft measurements and the corresponding COAMPS field along flight Leg 22. As indicated by the air-sea temperature difference (bottom right panel) this flight leg was also through a region of unstable stratification. Unlike Leg 1, the SST was very closely represented by the COAMPS on this leg, but, as with the flight Leg 1, the COAMPS air temperature was too cold. This cold bias of about 3 K caused the COAMPS sensible heat flux to be larger than that calculated from the aircraft measurements.

Another significant difference between the aircraft data and the COAMPS field was the wind speed variation along the leg. As is shown in the plot, the COAMPS winds got weaker towards point B, but the aircraft measurements show stronger winds toward point B. This is consistent with our discussion earlier regarding the relative position of the leg to the jet core since COAMPS misplaced the location of the jet axis too far north. The effect of these opposing wind speed trends is reflected in both the sensible and latent heat flux trends. It is also shown that the heat flux trends increase towards point B, closer to the jet, just as the wind stress trend would also indicate. However, it is shown that where the wind speeds are very close to point A, that the cold bias is what tends to cause the higher COAMPS heat flux results. This is again true for the latent heat flux even though the mixing ratio appears to be well represented. However, this accuracy in the mixing ratio representation is only coincidental. The higher mixing ratio content towards point B in COAMPS is due to the proximity of point B to the COAMPS represented southern leading edge as opposed to the aircraft measurements increasing due to the proximity of point B to the jet axis and higher winds.

The u and v wind components for COAMPS show winds shifting from northeasterly becoming more northerly towards point B. However, the aircraft

measurements show only a slight northerly turning of the winds along the leg. Again, COAMPS under predicts the turbulent kinetic energy.
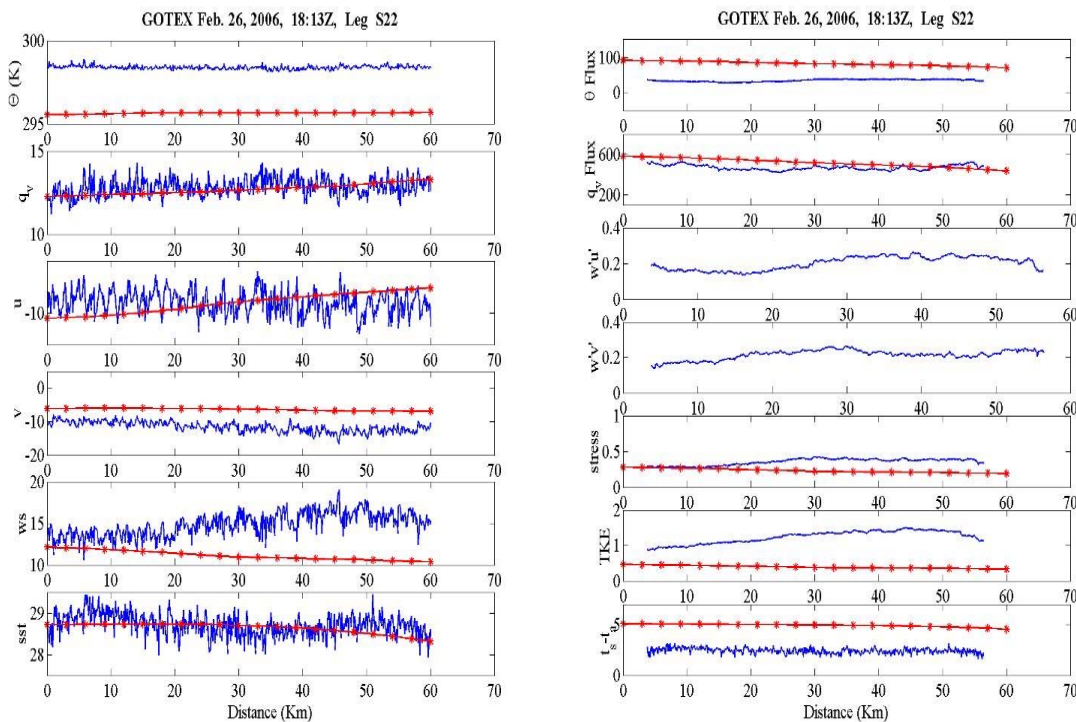
Figure 33.   Same as Figure 32, except for flight Leg 22.

2.   Stable Conditions

Flight Leg 7 is located in between Legs 1 and 22. As indicated by the air-sea temperature difference, the aircraft data suggests that this leg was made in a low-level stable regime. The COAMPS model, however, due to the cold bias of the air temperature and warm bias of the SST along this leg indicated an unstable stratification. The wind speed, direction, and mixing ratio all appeared to be well represented by COAMPS. The resulting flux calculations showed that COAMPS over predicted the sensible and latent heat fluxes to the atmosphere along the entire leg. The wind stress was also over predicted by COAMPS for most of the leg and turbulent kinetic energy was under predicted near point B. This discrepancy is evidently a result of the drag and exchange coefficients in the bulk aerodynamics formulation used in COAMPS.
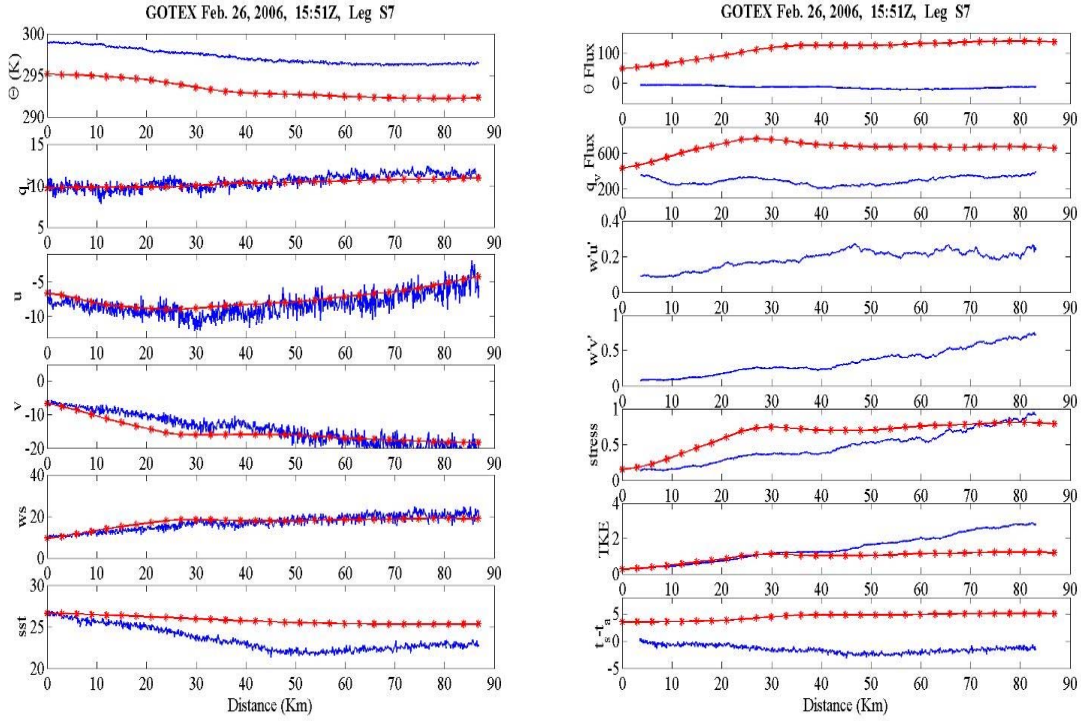
Figure 34.   Same as Figure 32 except for flight Leg 7.

3.   Temporal Comparison

After completing all the legs along the jet axis and returning to the gap exit region, the aircraft did another low-level pass over the same coordinates as for Leg 1. This second overpass occurred approximately 6 hours after the initial pass. The results of this pass (Leg 37) are plotted against the results of the first pass (Leg 1) in Figure 35. The data for Leg 37 was reversed to match the orientation of Leg 1, as well as being offset according to the flight coordinates so that the legs as viewed on the plot represent all the approximately same locations on the distance axis along the bottom. This was done to ensure that the comparison is made at the same location. Flight Leg 37 results are marked in green (COAMPS) and black (aircraft).

Many changes have occurred temporally along these legs located coastally near the gap exit. The potential temperature plot shows an increase in temperature for both the aircraft measurements and COAMPS. This supports the discussion that surface daytime heating over the landmass had increased the surface sensible heat flux and warmed the

low level air before it flowed over water as discussed in section 4. The COAMPS increase in temperature shows a three to four degree increase, whereas the aircraft shows only about a one to two degree increase. COAMPS is still too cold.

The mixing ratio also increases for both COAMPS and the aircraft measurements. COAMPS maintains an increasing moisture gradient towards the jet core and increases by up to about 1 g kg^{-1}, whereas the aircraft data shows up to a 3 g kg^{-1} increase over the western portion of the leg and a mild increase over the eastern portion which overall results in a fairly consistent mixing ratio over the entire leg of about 12 g kg^{-1}. COAMPS is still too dry.

The wind speeds remained fairly consistent over the 6 hour difference in observations. Small changes in direction include the aircraft measurements indicating a slightly larger easterly component towards the western edge of the leg and COAMPS veers the winds slightly more northeasterly over the entire leg.

The SST remained constant for the COAMPS run because the model was run with that limitation, but the aircraft measurements show that the SST does indeed change. The SST dropped by as much as 2 degrees with the most change near the western portion.

The trends for both the model and the measurements are consistent by showing warmer temperatures and higher mixing ratio values. The air-sea temperature difference plot (lower right) reflects these trends by indicating more stability. However, the aircraft measurements indicate that it has become a stable region, where as the overall cold bias of COAMPS continues to describe the low levels as unstable.

Considering the results just described, it makes sense that the sensible and latent heat fluxes decrease for both the model and aircraft data, but COAMPS continues to over predict both exchanges to the atmosphere. The turbulent kinetic energy also continues its model bias of estimating too little energy.

Figure 35.   Same as Figure 32 except for values for flight Leg 37 and its corresponding COAMPS values are plotted on the same line graphs. Red is COAMPS data from Leg 1. Blue is aircraft data from Leg 1. Green is COAMPS data from Leg 37. Black is aircraft data from Leg 37. Leg 37 data was spatially reversed so that it is correct relative to the endpoints that mark Leg 1 (e.g., the 0 km distance indicates the western endpoint).

VI. CONCLUSIONS AND RECOMMENDATIONS

A. SUMMARY AND CONCLUSIONS

The objective of this thesis is to understand the spatial and temporal variation of gap outflow over water and its interaction with the sea surface. Using the Navy's COAMPS model, the Tehuano event of 26 February 2004 was simulated. This Tehuano event was chosen because it was coincident with the GOTEX project in which a C130 aircraft operated by NCAR made data collection flights over the outflow region.

Horizontal and vertical structure of the outflow characterized by COAMPS was first compared to observations from satellite and local weather stations. Visible satellite imagery revealed that the southern progression of the leading edge of the outflow was not handled well by the simulation, however, the westward progression was. Also, a major cyclonic vortex that COAMPS had simulated southeast of the gap exit region was not confirmed by scatterometry comparisons. Further comparisons with the data collected by the aircraft revealed possible reasons for these discrepancies. The SST field of COAMPS was generally 1-2 degrees warmer than that observed by the aircraft at corresponding locations. Also, the initial fields of the simulation show the presence of local divergences along the southern leading edge which possibly could have resulted from mesoscale instabilities in the model. Furthermore, COAMPS air temperatures, both in and above the boundary layer, were too cold. This may have contributed to the surface pressure initialization adjustments that COAMPS experienced in which high pressure was simulated south of the outflow region. This possibly added an additional gradient force to the domain and prematurely turned the outflow winds toward the west. The higher surface pressures at initialization produced oscillations in the pressure field until approximately 18Z, the sixth hour after initialization, after which the model stabilized and showed potential of simulating the pressure ridge associated with the outflow extending farther south which would correspond to observations and previous studies.

The northern and western regions of the outflow did compare well with previous studies in wind direction and intensity as well as did the anticyclonic vortex structure to the right of the jet core. This region of the outflow was coincident with the aircraft

57

observations and was therefore useful in comparisons of the structure of the boundary layer and the air-sea fluxes. Also, the simulated jet core, when compared to the dropsonde data collected by the aircraft whose path was in close proximity of the actual jet core, showed similar structure and was determined useful in understanding the processes that occurred along the jet axis to the westward extending leading edge.

Analysis of the coastal outflow near the gap exit showed a pressure ridge, cool potential temperatures, an elevated jet core at the boundary layer top with lowered boundary layer heights, and strong vertical shear within the boundary layer. Return flow around the anticylonic region to the right of the jet produced a strong gradient in mixing ratio, winds, and a boundary layer discontinuity along its interface with the outflow.

The evolution of the outflow along the jet core showed strong dynamical forcing was the dominant influence on the structure of the outflow for the first 200 km with strong vertical shear, weak stratification, and a decreasing boundary layer thickness. After 200 km, as represented by both COAMPS and the dropsonde data, the boundary layer height increases, and temperatures, mixing ratios, and wind speeds are better mixed. This approximate 200 km length could be the point at which the strong dynamical dominance in controlling the boundary layer height yields to the turbulent processes in controlling the boundary layer height.

Data from specific low-level flight legs were used to calculate surface flux and turbulent properties of the lower boundary layer and compared against COAMPS. Whereas the winds were nearly identical and the atmospheric moisture content was closely represented, the temperatures of both the atmosphere and the sea surface showed a significant disparity. Spatially and temporally, however, the trends that were represented by COAMPS matched those of the GOTEX data for all variables and calculations. The exception was downstream where the jet core placement was misrepresented.

The difference in SST and in simulated air temperature results in large differences in the sensible heat and latent heat fluxes compared to the GOTEX data. In particular, COAMPS consistently showed unstable stratification in the entire outflow region whereas the GOTEX data showed that some regions were thermally stratified at low

58

levels. Yet turbulence remained strong over these stable areas suggesting the dominant forcing of vertical shear was generating turbulence along the jet core. The wind stress values also diverged in comparison. This indicates a need for improvement in the formulation of the drag and exchange coefficients and the surface roughness since the wind speed itself was well represented.

B.   RECOMMENDATIONS

Improved temperature representation is the first step in improving the model simulation of the boundary layer processes and surface flux calculations. Another consideration for better simulation is to include the ocean feedbacks, especially on the changing SST to accommodate the rapid development during a gap outflow event. Finally, a more in depth understanding of the boundary layer development could be achieved through mesoscale budget analysis.

This study focused on the Tehuano event of 26 to 27 February which coincided with the GOTEX project. Continued study of the outflow events that occurred in coincidence to the GOTEX project's 10 other flights during February of 2004 may lead to more unambiguous conclusions about the development of the boundary layer in high wind outflow conditions.

THIS PAGE INTENTIONALLY LEFT BLANK

LIST OF REFERENCES

Baines, P.G., 1995 : Topographic Effects in Stratified Flows. Cambridge University Press, 482 pp.

Bourassa M.A., L. Zamudio, and J. J. O'Brien, 1999: Noninertial flow in NSCAT observations of Tehuantepec winds. *J. Geophy. Res.* **Vol 104**, C5 11311-11319.

Chelton, D. B., M. H. Freilich, and S. K. Esbensen, 2000: Satellite observations of the wind jet off the Pacific coast of Central America. Part I: case studies and statistical characteristics, *Mon. Wea. Rev.*, **Vol. 128**, 1993-2018.

Chelton, D. B., M. H. Freilich, and S. K. Esbensen, 2000: Satellite observations of the wind jet off the Pacific coast of Central America. Part II: Regional relationships and dynamical considerations. *Mon. Wea. Rev.*, **Vol. 128**, 2019-2043.

Cobb, H. D., D.P. Brown, and R. Molleda, 2003, Use of Quikscat imagery in the diagnosis and detection of Gulf of Tehuantepec wind events 1999-2002 (2003-12SATMET), 12th Cong. On Interactions of the Sea and Atmosphere, Long Beach, CA, 8-13, Feb. 2003.

Clarke, A. J., 1988, Inertial wind path and sea surface temperature patterns near the Gulf of Tehuantepec and Gulf of Papagayo, *J. Geophy. Res.*, **V93**, C12, 15491-15501.

Federal Research Division, Country Studies, [available online at http://countrystudies.us/mexico/48.htm], last accessed September 2006.

Fleet Numerical METOC Detachment, Asheville NC., [available online at https://navy.ncdc.noaa.gov/], last accessed September 2006.

Gal-Chen, T., and R. C. J. Somerville, 1975: On the use of a coordinate transformation for the solution of the Navier–Stokes equations. *J. Comput. Phys.,* **17,** 209–228..

Gutierrez de Velasco, Guillermo and C. D. Winant, 1996, Seasonal patterns of wind stress curl over the Gulf of Mexico, *J. Geophy. Res.*, V101, No. C8, **18**,127-18,140.

Hodur, R. M., 1997, The Naval Research Laboratory's Couple Ocean/Atmosphere Mesoscale Prediction System(COAMPS), *Mon. Wea. Rev.,* **125**, 1414-1430.

Mass, C. F., S. Businger, M. D. Albright, and Z. A. Tucker, 1995: A windstorm in the lee of a gap in a coastal mountain barrier. *Mon. Wea. Rev.*, **123**, 315-331.

Nasa's Jet Propulsion Laboratory, California Institute of Technology, Education, [available online at http://sealevel2.jpl.nasa.gov/jr_oceanographer/oceanographer-chelton.html], last accessed September 2006.

Nasa's Jet Propulsion Laboratory, California Institute of Technology, Physical Oceanography Distributed Active Archive Center (PO.DAAC) , [available online at http://podaac.jpl.nasa.gov/], last accessed September 2006.

NOAA's Comprehensive Large Array-data Stewardship System, [available online at http://www.class.noaa.gov/nsaa/products/], last accessed September 2006.

Plymouth State Weather Center, [available online at http://vortex.plymouth.edu/], last accessed September 2006.

Stumpf, H.G., 1975: Satellite detection of upwelling in the Gulf of Tehuantepec, Mexico. *Mar. Wea. Log*, **19**, 71-74.

Steenburgh, W. J., D. M. Schultz, and B. A. Colle, 1998, The structure and evolution of gap outflow over the Gulf of Tehuantepec, Mexico, *Mon. Wea. Rev.*, **Vol. 126**, 2673-2691.

University Corporation for Atmospheric Research, Cooperative Program for Operational Meteorology, Education and Training, [available online at www.**comet**.ucar.edu/], last accessed September 2006.

University Corporation for Atmospheric Research, Project GOTEX, [available online at http://www.eol.ucar.edu/raf/Projects/GOTEX/], last accessed September 2006.

University of Wyoming, Department of Atmospheric Sciences, [available online at http://weather.uwyo.edu/upperair/sounding.html], last accessed September 2006

Wikipedia, [available online at http://en.wikipedia.org], last accessed September 2006.

INITIAL DISTRIBUTION LIST

1. Defense Technical Information Center
   Ft. Belvoir, Virginia

2. Dudley Knox Library
   Naval Postgraduate School
   Monterey, California

3. Chairman, Code 373
   Department of Meteorology
   Naval Postgraduate School
   Monterey, California

4. Professor Qing Wang, Code 373
   Department of Meteorology
   Naval Postgraduate School
   Monterey, California

5. Professor Wendell A. Nuss, Code 373
   Department of Meteorology
   Naval Postgraduate School
   Monterey, California

6. Shouping Wang
   Naval Research Lab
   Monterey, California

7. Carl Friehe
   Department of Mechanical Engineering
   University of California at Irvine
   Irvine, California

8. Kenneth Melville
   Scripps Institute of Oceanography
   University of California
   San Diego, California

9. LT Robin C Cherrett
   Monterey, California